Experimental investigation of the size effect in High Cycle Fatigue: role of the defect population in cast aluminium alloys

Driss EL KHOUKHI[1, 2, 3,*], Franck MOREL[1], Nicolas SAINTIER[2], Daniel BELLETT[1], Pierre OSMOND[3], Viet-Duc Le[1], Jérôme ADRIEN[4]

driss.el-khoukhi@ensam.eu

Tel : 0033648508178

[1]LAMPA, Arts et Métiers Paris Tech, 49 035 Angers, Cedex, France
[2]I2M, Arts et Métiers Paris Tech, 33170 Talence, Cedex, France
[3]Groupe PSA, 78955 Carrières-sous-Poissy, Cedex, France
[4]MATEIS, INSA de Lyon, 69621 Villeurbanne, Cedex, France

Abstract. Cast Al-Si alloys have been widely used in automotive applications with regard to their low density and excellent thermal conductivity. Many components made of these alloys are subjected to cyclic loads which can lead to fatigue failure. Furthermore, for these materials the well know size effect in fatigue, whereby the fatigue strength is reduced when the size is increased, can be significant and need to be properly evaluated. This paper analyses the role of casting defects on the fatigue strength's size effect sensitivity. A uniaxial fatigue testing campaign (R=0.1) has been conducted using two cast aluminium alloys, fabricated by different casting processes (gravity die casting and lost foam casting), associated with the T7 heat treatment, and with different degrees of porosity. The fatigue response of different specimens (smooth and notched) with different stressed volumes has been investigated. The first part of this article is dedicated to the experimental characterization of the size effect in both alloys via the concept of the Highly Stressed Volume. The second part investigates the effect of the Highly Stressed Volume on the critical defect size via Kitagawa-Takahashi diagrams. The results show that the magnitude of the size effect and the experimental scatter are strongly linked to the characteristics of the defect population present in the alloy. It is revealed that the alloy B, with a high density of pore and a population of defects with relatively large size, shows non-significant size effect and less scatter in fatigue strength. In comparison, alloy A that exhibits a low density of pore and a population of defects of relatively small size manifests significant size effect and high scatter in fatigue strength.

Keywords: HCF; size effect; microstructural heterogeneities; cast aluminium alloys; fatigue scatter.

1. Introduction

1.1 Context, introduction and objectives

The fatigue data transferability from laboratory specimens to real components or structures is very often difficult to handle because of the high number of parameters potentially affecting the fatigue strength. Besides the loading mode, the microstructural heterogeneities, the stress gradient and the size of the loaded volume can show significant effects on the fatigue strength.

In particular, it is generally accepted that the fatigue strength of certain materials decreases with an increase in the volume [1-2]. This is referred to as either the "volume effect", the "size effect" or the "scale effect" and is often simply explained by an increase in the probability of encountering a large material defect in the fatigue active volume. The effect is influenced by factors related to the distribution of defects in the material and the impact of the manufacturing process on the homogeneity of the material.

Kloos et al. [3] classified the size effect phenomenon into the following categories: (i) statistical size effect induced by the high probability of defects in larger specimens, (ii) geometrical size effect attributed to stress inhomogeneity from different notch types, this can also be referred to as the stress gradient effect, (iii) production size effect generated by production technology and (iv) surface size effect caused by the surface characteristics such as roughness.
Makkonen [4] proposed that the size effect, or the statistical size effect using Kloos' terminology, can be explained using the weakest link theory by Weibull [5]. Makkonen [4] showed the influence of the statistical size effect on the high cycle fatigue behaviour of both smooth and notched cylindrical specimens.

Regarding the gradient and the size effects, all the experimental investigations in the literature [6] tend to show that "the higher the stress gradient, the higher the fatigue strength" and "the higher the stressed volume size, the lower the fatigue strength". In High Cycle Fatigue (HCF) and as mentioned above, probabilistic approaches, based most of the time on the weakest link concept, manage to capture the statistical size effect whereas the stress gradient effect can be adequately modelled using a non local criterion [7–10]. It can also be shown that the fatigue strength scatter and the statistical size effect are most of the time closely related.

Many authors have investigated the effect of porosity on the propagation mechanisms [11–13]. Porosity is one of the main parameters in the fatigue life of cast alloys as it affects both crack initiation and propagation phases. Ammar et al [13] has shown that surface porosity is the most important casting defect that affects fatigue life; it acts as the most likely site for crack initiation since 92% of all tested specimens fractured because of surface porosity acting as a crack initiation site. The fatigue life of the sample decreases as surface pore size increases, and vice versa. Nevertheless, it should be kept in mind that the objective here is to study the scalability and geometric size effect using the Highly Stressed Volume (HSV) concept in terms of the fatigue strength distribution, corresponding to the stopping criterion used experimentally (frequency drop of -1 Hz). This criterion corresponds to fatigue cracks of approximately 2 mm in length on the surface of the specimens. Note that the specimens were not broken in half. From this point of view, the main difference in fatigue resistance is attributed to the defect size and its shape well as its location. These parameters control the magnitude of the size effect. This approach is motivated by the fact that the PSA Group use a fatigue design strategy based on the Strength-Resistance method [14].

Even though the experimental observations of the size and the gradient effects concern the macroscopic fatigue response, a few studies [7, 9–11] try to show how microscopic features like microroughness or microdefects can affect the global stress gradient and size effects. The idea is, from some statistical distributions of surface or volume defects, to derive the macroscopic fatigue strength distribution. When doing so, three main difficulties arise. First, the mechanisms of crack initiation must be known to identify which of the microstructural features are responsible for fatigue damage and hence which statistics must be described. The task is all the more tough when several damage mechanisms are active [12, 13]. Second, the experimental description of the statistics must be carried out by using a relevant representative volume. The question is here to know what is the minimum size of the fatigue representative volume (FRV) and how this FRV is affected by the microstructure features distribution. Third, when the main fatigue damage mechanisms have been identified, the relation between the microstructural heterogeneities characteristics (size, shape …) and the fatigue strength levels must be estimated. The Kitagawa diagram is for instance largely used in fatigue to relate the fatigue strength to the defect size.

The work presented in this paper aims at getting a better understanding of how the highly stressed volume and the defect population affect the macroscopic fatigue response.
It focuses on cast Al-Si alloys, widely used in the automotive industry. In order to manufacture engine components, the Groupe PSA indeed uses two foundry processes that result in components containing Microstructural Heterogeneities (MH), principally shrinkage pores and oxides, with different characteristics (size, shape and spatial distributions). These components are subjected to cyclic mechanical loads (in the High Cycle Fatigue regime) that can result in the appearance of cracks and thus lead to the failure of the structure. The effect of the MH on the fatigue behaviour has been well documented in references [13, 16 -19].

A typical engineering design practice [24] involves the identification of a fatigue criterion, used to size and validate real components, based on tests carried out on laboratory sized specimens, generally under simple loading modes (e.g. tension, bending, and torsion). However, real component loading conditions are often different to those applied to laboratory test specimens, particularly in terms of the size of the critical zone (i.e. size effect) and the homogeneity of the stress state in this zone (i.e. stress gradient effect). Hence, the industrial objective of this work is to develop predictive tools to ensure the passage from an elementary volume to the structure, taking in account the size effect and the stress gradient effect. In this work, the effect of microstructural heterogeneities, principally shrinkage porosity and oxides, on the statistical size effect in cast Al-Si alloys is investigated.

An example of fatigue design approach taking account the size effect is the Highly Stressed Volume (HSV) approach who was first introduced by Kuguel [25] in 1961, and then employed by Sonsino and Fischer [26], and Lin and Lee [27]. The terminology Vn% is used to define the volume of material that is subjected to at least n% of maximum principal stress ($\sigma n\% = n\% \times \sigma max$). This volume of material is assumed to have an increased probability of fatigue crack initiation. The percent is assumed to be 95% by Kuguel [25] and 90% by Sonsino and Fisher [26]. The concept has been verified for metallic components with good success using the V90% volume [14]. For short-fiber reinforced specimens and components, a value of V80% proved to be more appropriate than V90% [28]. The effect of HSV on the fatigue behaviour has been well documented in references [25–27].

Due to its significance in structural reliability, certain design standards require the size effect to be taken into consideration. As an example, for the design fatigue curves of the ASME B&PV Code [25–27], the factors of 2 (stress) and 20 (cycles) are adjustment factors applied to the small–specimen data to obtain reasonable estimates of the lives of actual reactor components. These factors were intended to account for data scatter (including material variability) and differences in surface condition and size between the test specimens and actual components.

Two Al-Si alloys with different porosity distributions are chosen in order to understand how the characteristics of the defect populations affect the statistical size effect. Computed Tomography analyses are conducted in order to characterize the porosity in terms of size, shape and spatial distributions in these alloys. Different specimen shapes, including both smooth and notched specimens are machined from these alloys, in order to obtain geometries with different Highly Stressed Volumes. High cycle fatigue tests are conducted to investigate the size effect on the fatigue strength using the HSV concept. Finally, fractographic analyses are conducted to investigate the relationship between the critical defects and the fatigue strength via the Kitagawa-Takahashi diagram. Statistical analyses of fatigue data are also presented.

It is important to stress that 140 samples have been tested in order to get a good approximation of the statistical distribution with a high level of confidence.

2. Materials and experimental conditions

2.1 Mechanical and Material Properties

To study the influence of casting defects on the statistical size effect, two primary cast aluminium alloys, referred to as alloys A [AlSi7Cu05Mg03-T7] and B [AlSi7Mg03-T7], have been used (see Figure 1). These alloys were fabricated by different casting processes (alloy A: gravity die-casting and Alloy B: lost foam casting), and subject to the T7 heat treatment. These processes result in different porosity populations (i.e. volume fraction, defect size…) and different mechanical properties [see table 1 and table 2]. Previous works concerning the characterization of these materials have been done by Le [17] and Koutiri [20].

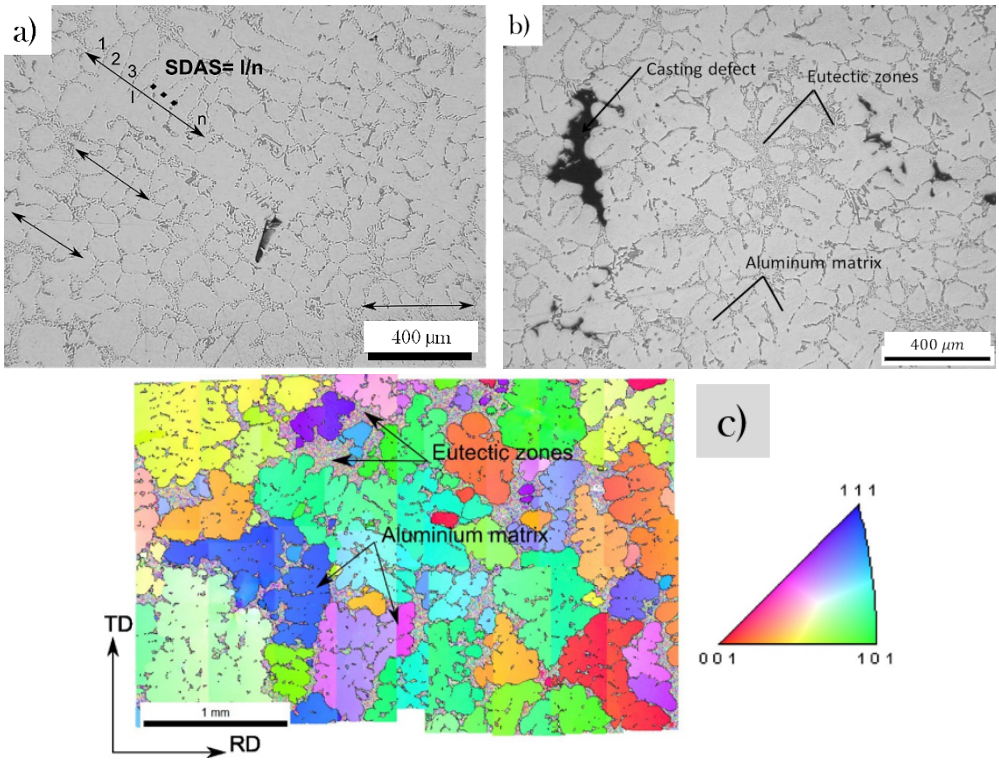

Figure 1: The microstructure of the investigated alloys (a) Alloy A (AlSi7Cu05Mg03 - T7) (b) Alloy B (AlSi7Mg03 - T7) and (c) Grain map showing grains for alloy A with $\sqrt{\boldsymbol{Area}\ (\boldsymbol{grain})} = 337 \pm 143$ µm.

Table 1 summarizes the mechanical and microstructural properties of these alloys [13, 16].

Table 1: Properties of the investigated cast Al-Si alloys

Grade	Alloy A	Alloy B
Designation	AlSi7Cu05Mg03 - T7	AlSi7Mg03 - T7
Chemical composition (wt %)	7% Si, 0.3% Mg, 0.5% Cu, Al Rem.	7% Si, 0.3% Mg, Al Rem.
Casting Process	Gravity Die	Lost Foam
Heat treatment	T7	T7
SDAS (µm)	42±10	77±19
Young Modulus E (GPa)	77±6 [16]	68±5 [16]
Yield stress $\sigma_{Y0.2\%}$ (MPa)	260±2	240±5
Ultimate tensile strength σ_u (MPa)	304±4	251±6
Elongation A (%)	4.7±1.2	0.8±0.1
Porosity (%)	0.03	0.28
Micro-hardness (Hv25Gr)	115	100

From Table 1, we conclude that the materials do not show a large difference in terms of micro-hardness, yield stress, ultimate strength and Young Modulus. Nevertheless, in terms of the SDAS parameter and Elongation, a significant difference is observed. However, it is well known that the uniaxial fatigue resistance in the HCF regime is mainly controlled by the defect size [13, 16, 28 – 30]. Therefore, in this work, it is assumed that the SDAS and Elongation are not the main parameters controlling the fatigue response.

2.2 Porosity Analyses

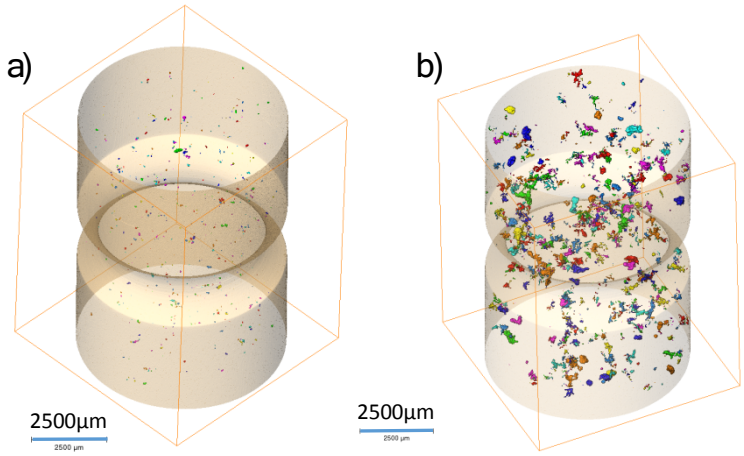

Figure 2: Micro-tomography scans of the alloys (a) A alloy and (b) B alloy

In order to characterize the defect size distribution in these alloys, Computed-Tomography (CT) analyses were undertaken. CT scans were done by the MATEIS laboratory at INSA Lyon with resolution of 8 µm/voxel. The AVIZO software was then used in order to analyse the raw data. The alloys were characterised in terms of size and shape distributions of their micro-shrinkage porosity. Also, the distance between each individual pore was determined. An inspection volume of 363 mm^3 was used. Figure 2 illustrates the defect population as imaged by microtomography on two notched fatigue specimens (see section 2. 4 for more details on specimen geometry). It can be clearly seen that alloy B has considerably higher density of large pores when compared to alloy A.

With the CT scans, only pores in the scanned volume can be observed. However, oxides are also potential sites of crack initiation. Nevertheless, as the experimental results show, the dominant mechanism of failure is the one that starts from a pore. Therefore, to understand the effect of microstructural heterogeneities on the fatigue size effect, it seems sufficient to understand the effect of the porosity on the fatigue size effect.

Figure 3 shows the defect size distributions for the two alloys in terms of the equivalent Murakami parameter [52], $\sqrt{Area}_{eq}$ of the defect. The relationship between pore volume obtained by tomography and its equivalent square root of the projected area is given in Eq. 1. This relationship is obtained by assuming a spherical pore shape.

$$\sqrt{Area}_{eq} = \pi^{1/6} \left(\frac{3V}{4}\right)^{1/3} \quad (1)$$

The use of this approximation makes it possible to compare the sizes obtained by the CT scans and those measured on the fatigue failure surfaces.

The maximum pore sizes in terms of the $\sqrt{Area}_{eq}$ parameter, obtained in the scanned volumes, are 166 µm for alloy A and 302 µm for alloy B. Almost the entire population of the defects in alloy A have a $\sqrt{Area}_{eq}$that is lower than 100 µm whereas 20% of the defects in alloy B have a $\sqrt{Area}_{eq}$ greater than 100 µm.

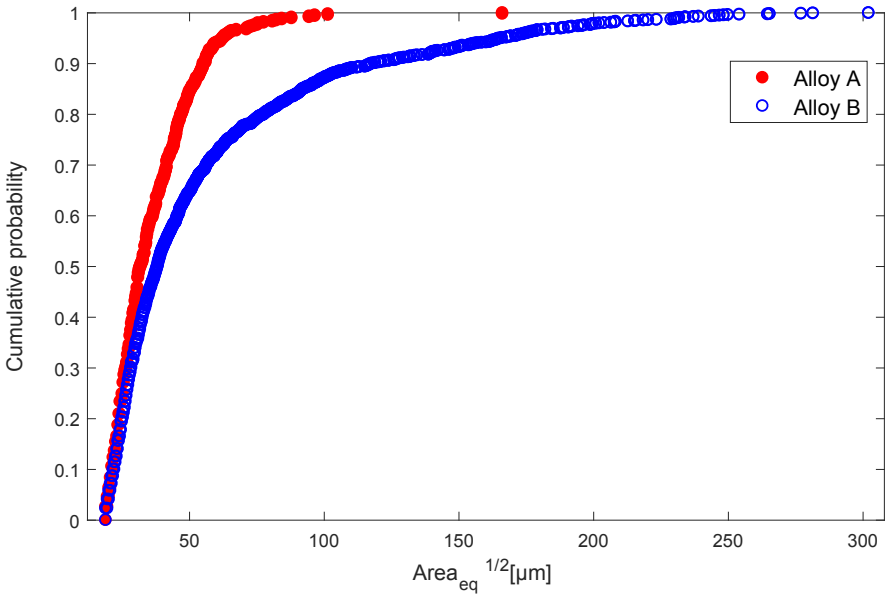

Figure 3: Distributions of the defect size of the pores from the scanned specimens in Fig. 2

In order to characterize the shape of the defects, the sphericity parameter is defined in equation Eq. 2.

$$S = \frac{\pi^{1/3}(6V)^{2/3}}{A} \tag{2}$$

where A is the surface area of the pore and V is the pore volume. This parameter compares the shape of a pore to a sphere. Only the perfect sphere will have a sphericity of 1.

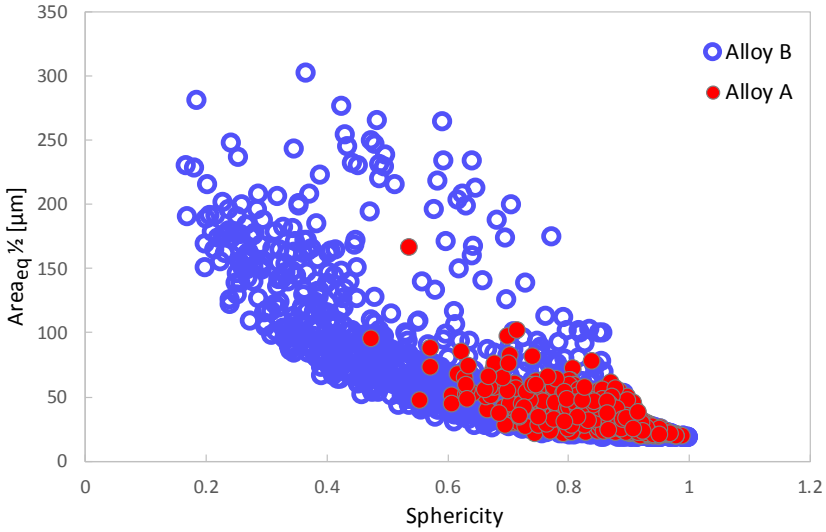

Figure 4: Defect size as a function of the sphericity of the defects

Figure 4 shows the relationship between pore size and sphericity for both alloys. It can be seen that the largest pores have the lowest sphericity and a complex shape. This tendency has also been observed in the previous works [13, 29, 31]. According to Buffiere classification [29, 31], this repartition tend to indicate the presence of shrinkage porosity and gas pores. This last type of pores seems especially present in the alloy B.

In order to characterize the spatial distribution of the pores in the scanned volume, the data obtained from CT scans were used to evaluate the distance to its nearest neighbor is established using the fact that the distance between the centers of mass of two pores P and Q, with Cartesian coordinates respectively (p1, p2, p3) and (q1, q2, q3), is:

$$d_T(P,Q) = \sqrt{(p_1 - q_1)^2 + (p_2 - q_2)^2 + (p_3 - q_3)^2} \quad (3)$$

The nearest-neighbor distribution is the distribution of distances from each pore P to its nearest neighbor in the scanned volume. The nearest neighbor distance is defined by Eq. 4 (see [39], [40] for more details).

$$d_P = \min_{Q \in X \setminus \{P\}} d_T(P,Q) \quad (4)$$

Where X is the scanned volume. The characteristics of this distribution are summarized in Table 2 where the coefficient of variation is defined as the ratio of the standard deviation to the mean.

Table 2: Characteristics of the defect distributions from scanned volumes of 363 mm^3

	Alloy A [Nb of pores = 454]			Alloy B [Nb of pores = 1569]		
	$\sqrt{Area}_{eq}$ [µm]	Sphericity	Nearest Neighbor [µm]	$\sqrt{Area}_{eq}$ [µm]	Sphericity	Nearest Neighbor [µm]
Min	20	0.48	60	20	0.17	40
Max	170	0.99	1200	300	1.00	1200
Mean	40	0.85	350	60	0.71	160
Median	35	0.87	180	40	0.76	120
Standard deviation	20	0.09	260	50	0.20	130
Coefficient of variation	0.43	0.09	0.83	0.83	0.24	0.86

Table 2 shows that the alloys have different characteristics in terms of size, shape and nearest-neighbor distance.

We can summarized the data contained in the table as follows:

- Defects size :
  - The mean of the defects size contained in ally B is 1.5 times higher than the mean of those contained in alloy A.
  - Either the coefficient of variation and the standard deviation for alloy A are lower than for the alloy B
- Nearest-neighbor distance :
  - The mean of the nearest-neighbor distribution for alloy A is two times higher than the mean of the alloy B.
  - The coefficients of variation of the nearest neighbor distributions of these alloys are almost the same.
- Defect shape :
  - The alloy A presents more regular shaped pores compared to those in the alloy B.

The characteristics of the defect size and nearest-neighbor distributions is likely to control the magnitude of size effect and scatter in these alloys.

2.3 Experimental conditions of the fatigue tests

All fatigue tests were performed under uniaxial tensile loads with a stress ratio R = 0.1 using a Rumul Testronic resonant testing machine at approximately 100 Hz. The stopping criterion was a drop in the resonance frequency of 1 Hz, corresponding to the presence of a fatigue crack of approximately 2 mm on surface. All tests were performed at room temperature, in air. The tests were conducted following the staircase method with a maximum life of 2x10^6 cycles. The run-out specimens were retested until failure at higher load levels in order to identify the critical defect that initiates a crack. A step of 5 MPa stress amplitude was used in the staircase procedure.

2.4 Specimens geometry

To study the effect of stressed volume on the fatigue strength of alloys A and B, different fatigue specimen geometries were defined, corresponding to different loaded volumes. These are shown in Figure 5 and are referred to as: “V1-Small Volume”, “V2-Reference Volume”, “V3-Large Volume” and “VN-Notched specimen”.

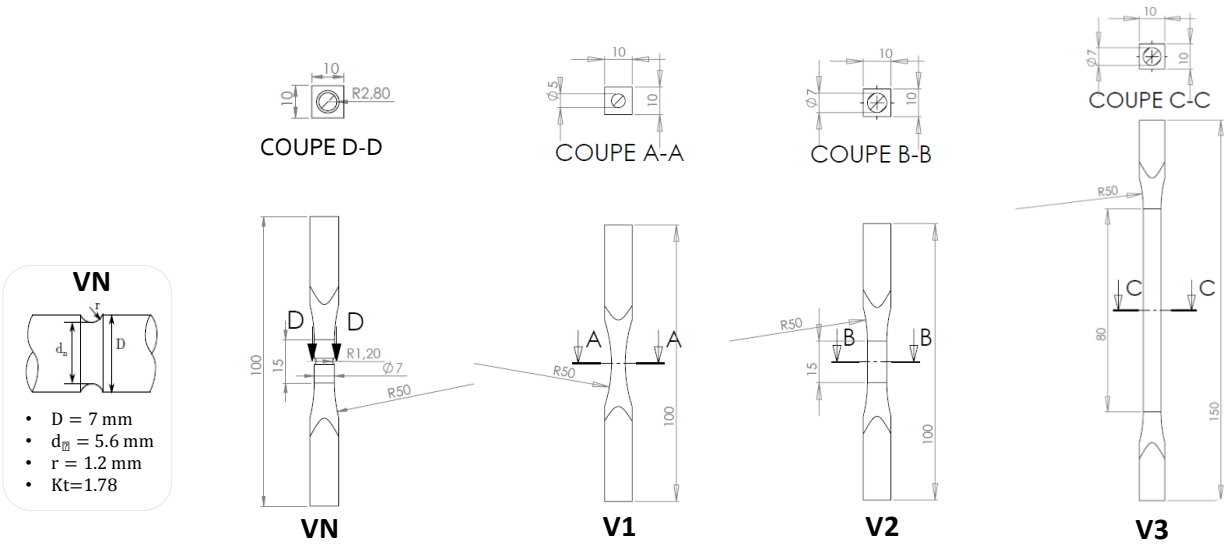

Figure 5: Specimens for tensile fatigue tests

2.5 Estimation of the Fatigue Active Volume “FAV”

To illustrate the difference between the four specimen shapes in terms of loaded volume, the concept of the Fatigue Active Volume “FAV” is used in an empirical manner.

In the following sections, the FAV is estimated using the combination of two criteria:

- Damage mechanism. In the literature, much works [13, 17, 28, 30, 34–36] have shown that the fatigue failure usually occurs at defect or pores located on the surface or in a sub-surface layer. In the experimental work undertaken in this work, the crack initiation sites are located in a subsurface of 500 µm for alloy A and 650 µm for alloy B. Figure 6 shows a subsurface pore with the depth ‘t’ in the crack initiation zone for alloy B. Figure 7 shows the cumulative distributions distance from the surface for all pores observed in the crack initiation zones in these alloys.

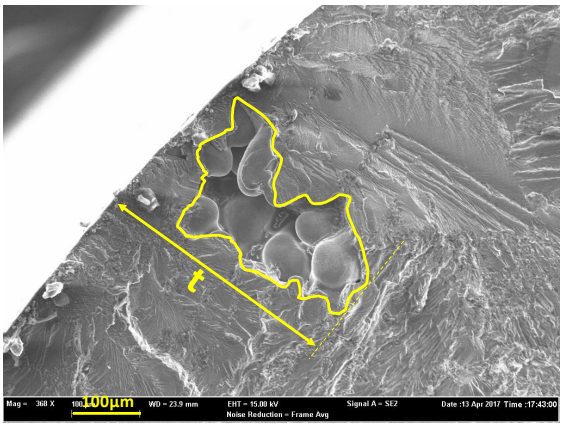

Figure 6: The definition of the depth of a critical defect

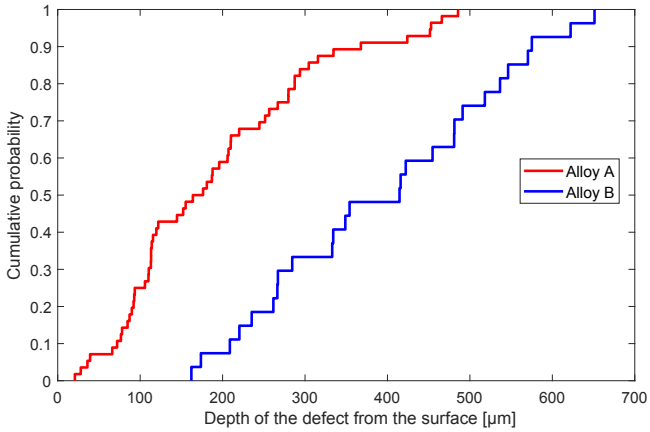

Figure 7: Cumulative probability of the defect depths for the alloy A and B

- Stress heterogeneity. A Highly Stressed Volume of V80% is chosen. The justification for choosing this value is based on the results for the V1 specimen, which has an hourglass shape (Figure 9). Most of the fatigue cracks in these specimens do not occur in the centre of the specimen where the cross-sectional area is the smallest and the stress is the highest. This is because the cast aluminium materials investigated are defect containing materials. Figure 9 shows the case of a specimen in which the fatigue crack is located approximately 5.82 mm from the middle of the specimen. Figure 8 shows the normalised stress at the crack location as a function of the distance from the centre of the specimen. From this figure, it can be seen that almost all of the specimens have failed at a stress level that is greater than 80% of the maximal stress.

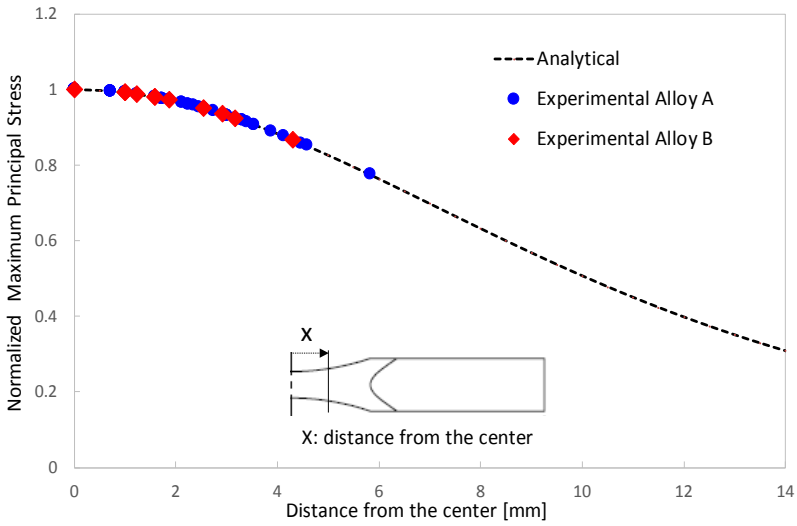

Figure 8: Fatigue crack localization in the hour-glass shaped V1 specimens

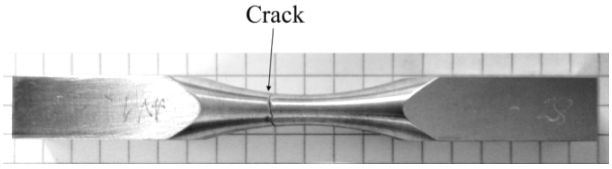

Figure 9: A-V1 specimen showing that the fatigue crack is not necessarily located in the center of the specimen

The combination of these two criteria is used to define the Highly Stressed Volume corresponding to $0.8\sigma_{Imax}$ located in a subsurface layer of thickness 500 µm for alloy A and 650 µm for alloy B. In the following section, this definition is referred to as the FAV. For each specimen geometry, an estimation of the Highly Stressed Volume has been done using finite element computation with a linear elastic analysis. Figure 10 shows FAVs identified for each case.

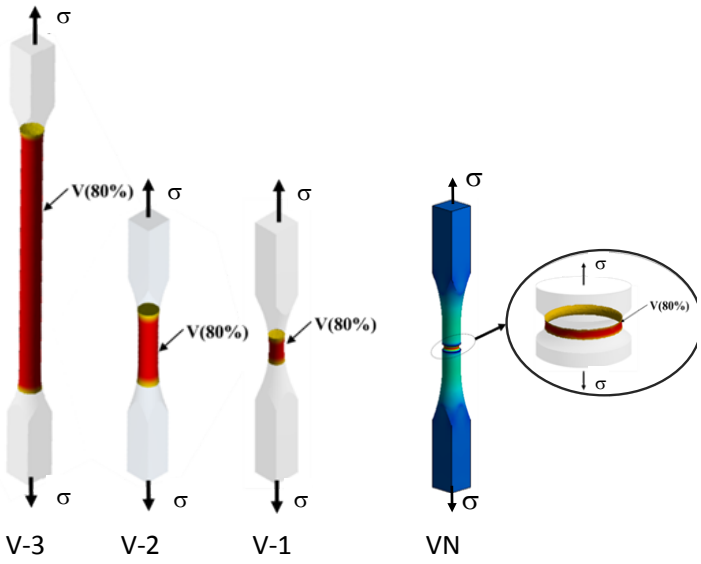

Figure 10: Highly Stressed Volume for (a) smooth specimens V1, V2 and V3 and (b) notched specimens

The use of the notch for the fatigue specimens VN has been designed to get a very small active volume.

In the following sections, we will use the estimated FAV_A for alloy A and FAV_B for alloy B. The FAV corresponding to each specimen shape, as well as stress concentration factors and number of specimens tested for each configuration, are presented in Table 3. We point out also that the FAV of the sample V3 for alloy B is not indicated in table 3 since it was not tested for this alloy. The stress concentration factors Kt were estimated as follows:

$$K_t = \frac{\sigma_{max}}{\sigma_{nom}}$$

Where, σ_{max} being the maximum elastic normal stress in the axial direction at the notch tip, and σ_{nom} is the nominal elastic stress based on the net section.

Table 3: Characteristics of the samples

Specimen	Number of specimens		Kt	FAV_A in mm^3 for the sublayer of 500 µm	FAV_B in mm^3 for the sublayer of 650 µm
	Alloy A	Alloy B			
VN	5	5	1.78	5	6
V1	47	11	1	90	110
V2	46	11	1	375	450
V3	12	0	1	1020	-

3. Fatigue SN curves and effect of FAV

3.1 High cycle Fatigue S-N Curves

High-cycle fatigue tests have been performed on specimens with different geometries taken from two Al–Si cast aluminium alloys. S–N curves have been represented to characterize the statistical size effect in these alloys. For the sake of simplicity, only the results corresponding to the standard volume V2 and the small volume V1 are shown for both alloys. Fig. 10 shows the S-N curves for these volumes: A-V1, A-V2, B-V1 and B-V2. The average S-N curves have been fitted to the experimental data using a power law based on the least square method.

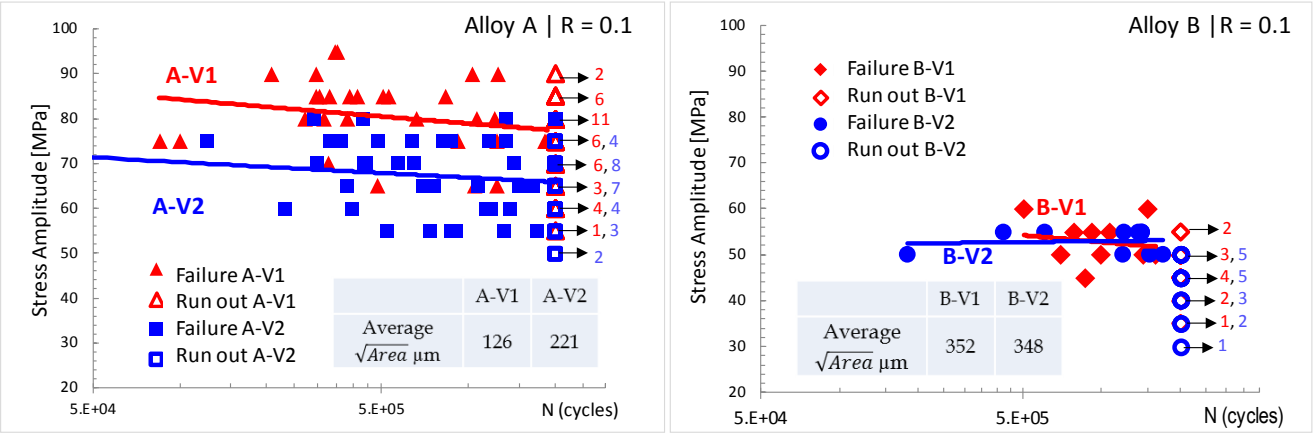

Figure 11: SN-Curves plotted in semi-Linear diagram for the batches A-V1, A-V2, B-V1 and B-V2

From Figure 11, it can be seen that there is:

- A large difference between the A-V1 and the A-V2 data. This indicates a significant size effect in alloy A,
- For alloy B, the data for B-V1 and B-V2 are almost superimposed. Hence, the size effect is almost negligible for alloy B,
- Less scatter in terms of fatigue strength is observed for alloy B data compared to alloy A data,
- The mean fatigue resistance for alloy B is lower than that of alloy A. This difference can be associated to the difference in terms of Cu cotenant and the critical defects size between the studied alloys. Work is underway which aims to evaluate the effect of Cu on the fatigue strength.

From these remarks, it can be concluded that alloy A shows a strong statistical size effect as compared to alloy B, at least for the range of investigated volumes.

3.2 Statistical size effect

In order to illustrate the influence of the size effect on the fatigue strength, the product of the nominal stress amplitude σ_D and stress concentration factor K_t is used. That is, for the notched specimens the local stress amplitude at the notch-tip is used. In references [37, 38], it was shown that there is a good correlation between the fatigue strength expressed as $K_t\sigma_D$ and the highly stressed volume. In this work, the correlation will be made in terms of the Fatigue Active Volume. Note that the notched specimens were designed to ensure minimal local plasticity at the notch-tip. At the highest loads experimentally applied for 5 specimens the von Mises stress exceeds the yield strength by 4%. Hence, the effect of cyclic plasticity is considered negligible. Let us also notice that the estimation of the fatigue limit of each specimen is assessed using the following formula proposed in [46].

$$\sigma_D = \sigma_{n-1} + (\sigma_n - \sigma_{n-1}) \times \frac{N_f}{2 \times 10^6} \quad (5)$$

where σ_D is the interpolated fatigue limit at 2 millions of cycles. σ_{n-1} is the stress amplitude level of the block prior to the block where failure occurs. For the specimens that fail at the first level (σ_n) of stress we supposed the existence of a fictive level (σ_{n-1}). σ_n is the maximum stress level of the final block of cycles during which failure occurs, and Nf is the number of cycles to failure in the final loading block. The main objective here is to get the fatigue limit of each specimen and not for the whole batch.

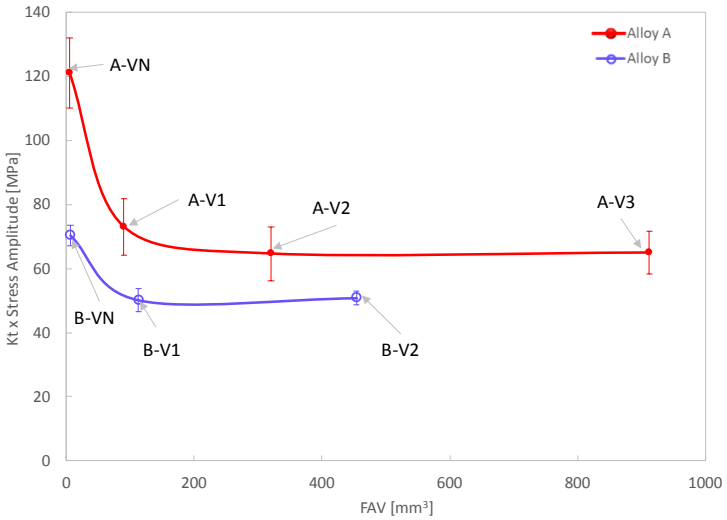

Figure 12: Local stress amplitude at fatigue limit as function of critical volume for alloys A and B

Figure 12 shows the effect of the fatigue active volume (FAV) on the local fatigue strength amplitude $K_t\sigma_D$ for 50% probability of failure for a stress ratio of R=0.1 at 2×10^6 cycles. For both alloys, the local fatigue strength amplitude decreases with increasing FAV, then stabilizes for each alloy at a specific FAV. The notched specimens show the highest strengths in terms of the local stress amplitude.

Following these observations, it can be concluded that:

- the alloy A has a more pronounced volume effect than alloy B. This is probably due to the characteristics of the defect population (i.e. pore size, distance between large pores, etc.…).
- for alloy A, the fatigue strength stabilizes from a specific volume of 375 mm³. This could be considered as the Fatigue Representative Elementary Volume (FREV).
- for alloy B, the fatigue strength stabilizes rapidly at a specific volume of 110 mm³, which can be considered as the FREV.

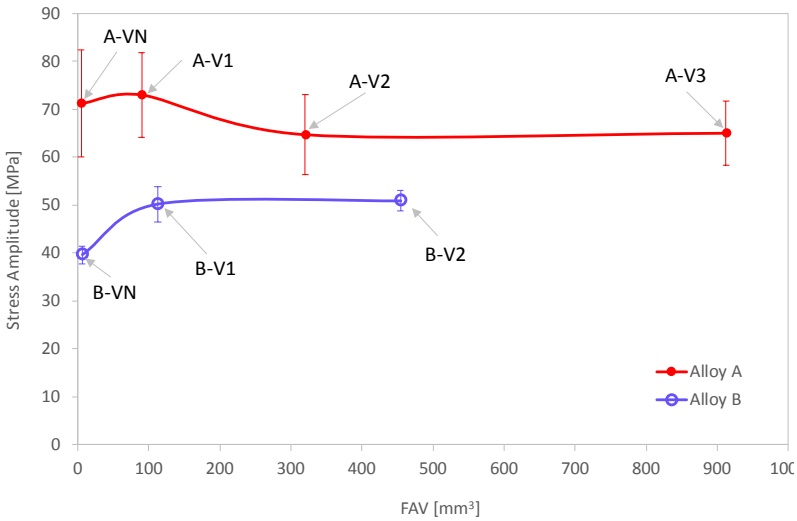

Figure 13: Nominal stress amplitude as function of critical volume for alloys A and B

Figure 13 shows the same data as Figure 12 but in terms of the nominal stress. It can be seen that for alloy B the presence of the notch in the B-VN specimens dramatically decreases the fatigue resistance as expected. However, for alloy A, the introduction of the notch caused the increase of the fatigue strength of the specimen A-VN compared to the specimen A-V2. This seems to indicate that for alloy A the volume effect is dominant compared to the notch effect.

3.3 Crack initiation Mechanisms

After fatigue failure, the crack initiation sites were systematically observed on all specimens. Different defect types were identified to be at the origin of fatigue crack initiation and are discussed below. SEM was used to measure Murakami parameter $\sqrt{\text{Area}}$ of the critical defects on the fatigue failure surfaces.

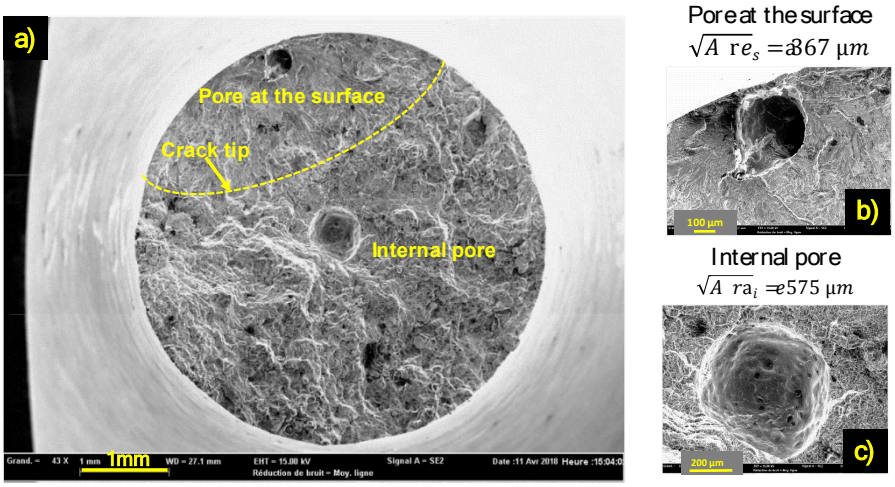

Figure 14: Fatigue failure, specimen B-V1-05, Sa= 55 MPa, Nf=919402 cycles, (a) Macroscopic view, detailed view of (b) surface pore and (c) internal pore

Figure 14 highlights the importance in fatigue of the free surface [37]. For this specimen, a very large defect can be seen in the middle of the specimen ($\sqrt{Area}$=575 µm) and a smaller one is visible near the surface ($\sqrt{Area}$=367 µm). The SEM observations clearly show that the smaller pore close to the surface is responsible for the fatigue failure.

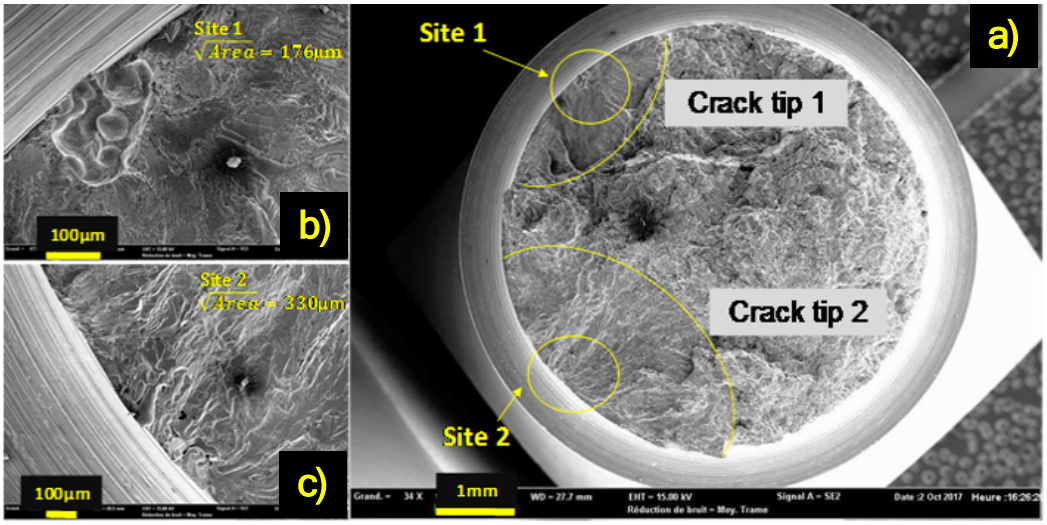

Figure 15: Specimen with multiple crack initiation sites, specimen B-NV-04, Sa=45MPa, Nf=129663 cycles, crack initiation from a pore at surface (a) Macroscopic view, detailed view of (b) gas pore and (c) micro-shrinkage pore

For four notched specimens of alloy B, the fatigue failure surfaces show two initiation sites (Figure 15). This reflects the higher density of large pores in alloy B even with a small Fatigue Active Volume. The size of the critical defects for the batch B-VN is summarized in Table 4.

Table 4: Critical defects for notched specimens of the alloy B

Specimen	√Area : Site 1 [µm]	√Area : Site 2 [µm]
B-VN 01	176	248
B-VN 02	243	333
B-VN 03	204	320
B-VN 04	176	330
B-VN 05	313	-

For alloy A, which has a lower pore density, other crack initiation mechanisms were observed such as initiation from oxides, Persistent Sleep Band (PSB) and even the combination of the two mechanisms (see Figure 16, Figure 17 and Figure 18). However, the dominant fatigue damage mechanism is crack initiation and growth from pores. Note that these damage mechanisms are fully consistent with those observed by Le [17] on specimen V2 under a load ratio R=-1. The statistics of crack initiation sites in these alloys are summarized in Table 5.

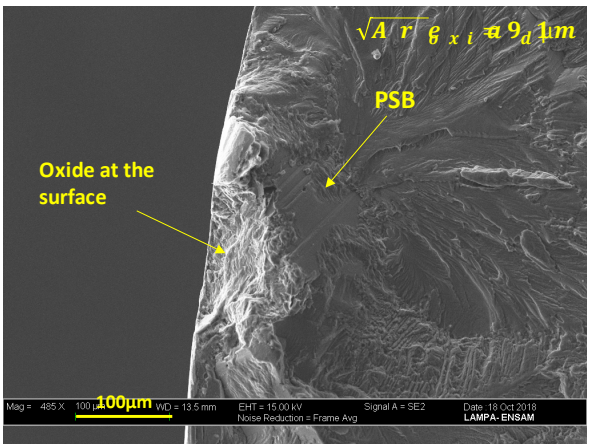

Figure 16: Crack initiation site with the combination of two mechanisms, specimen A-V1-29, Sa=75 MPa, Nf=328135 cycles, crack initiation from an oxide at the surface and persistent slip band (PSB)

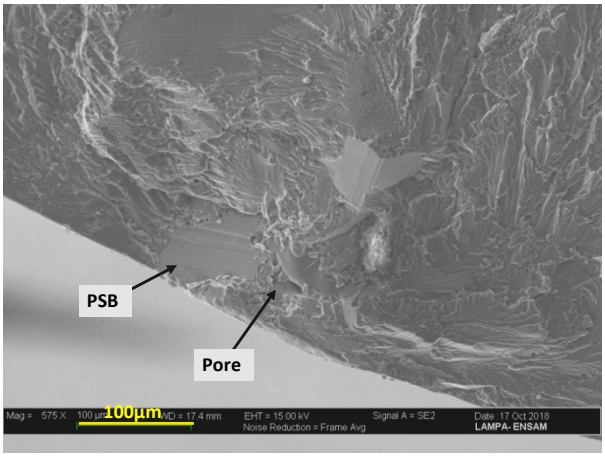

Figure 17: The presence of some sites with the combination of two mechanisms, crack initiation from persistent slip band (PSB) and pore near to the surface

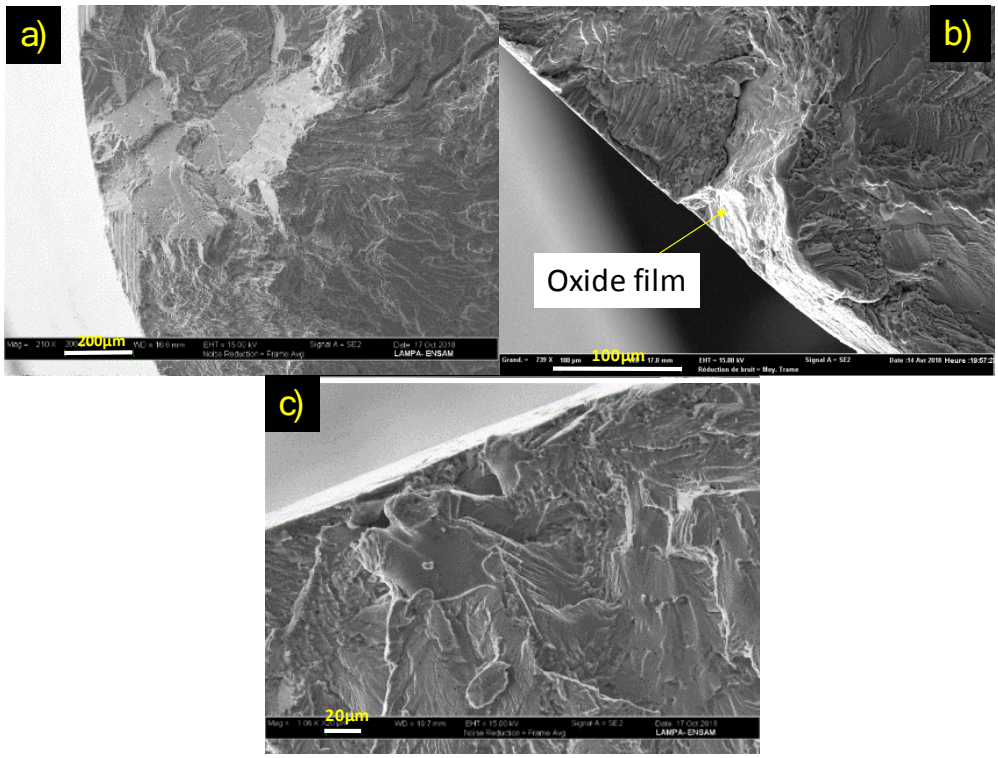

Figure 18: Other typical crack initiation mechanisms, (a) specimen A-V1-44, Sa= 85 MPa, Nf= 545162 cycles, crack initiation from persistent slip band (PSB), (b) specimen A-V2-17, Sa= 70 MPa, Nf= 441454 cycles, crack initiation from an oxide at the surface, and (c) specimen A-V1-43, Sa= 65 MPa, Nf= 1581225 cycles, crack initiation from pore at the surface

Table 5 summarizes the fatigue damage mechanisms determined via SEM observations of the failure surfaces for all tested specimens. For alloy A it can be seen that by decreasing the FAV size from A-V3, to A-V2 then A-VN, the percentage of non-pore related mechanisms increases. For alloy B, the only mechanism is failure from pore.

Table 5: Statistics of fatigue initiation sites for HCF

Mechanisms \ Batch	A-VN	A-V1	A-V2	A-V3	B-VN	B-V1	B-V2
Pore at the surface	2	21	23	12	5	10	11
Sub-surface pore	0	4	0	1	0	1	0
Internal Oxide (or inclusion)	0	0	0	0	0	0	0
Oxide (or inclusion) at the surface	1	3	8	0	0	0	0
PSB	1	6	2	0	0	0	0
PSB + pore	0	1	0	0	0	0	0
Oxide (or inclusion) + pore	0	6	5	0	0	0	0
Oxide (or inclusion) + PSB	1	6	1	0	0	0	0
Number of observed specimens	5	47	39	13	5	11	11
Percentage of mechanisms initiated from Pores (%)	40	53	59	100	100	100	100

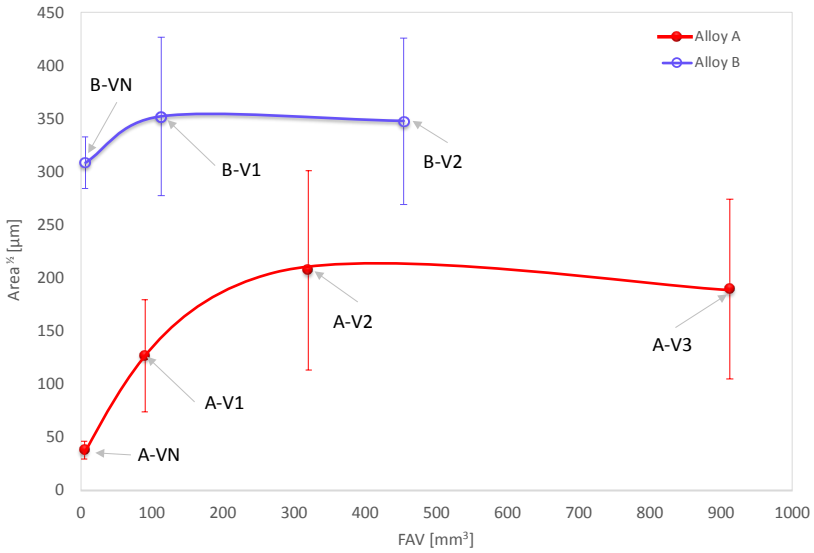

Figure 19: The critical defect size as a function of the Fatigue Active Volume

Figure 19 shows the evolution of the critical defect sizes expressed in terms of ($\sqrt{Area}$) as a function of the fatigue active volume for both alloys. The mean value of critical defect size in alloy B are larger than 300 µm. On the other hand, for alloy A, the mean value of critical defect size are less than 210 µm. The two curves show the same tendencies. For a small FAV, the average critical defect size is low. It starts to increase and then stabilizes for a FAV of approximately 110 mm³ for alloy B and a FAV 375 mm³ for alloy A. The average of critical defect size is 4 times for the notched specimens A-VN when compared to the stabilized volume. Nevertheless, the alloy B does not show the same level of increase. The difference in the average of critical defect size between the notched specimen B-VN and the stabilized volume is only 50 µm.

The postulate made by Weibull [5], i.e. the size effect is explained by an increase in the probability of encountering a large defect in large volume, seems to apply in alloy A but not in alloy B. The size effect in alloy A is very noticeable in contrast to what happens in alloy B. The following sections give further details on the quantification of the magnitude of size effect in these alloys.

3.4 First quantitative approach of size effect

In this section, we aim to quantify the magnitude of size effect present in the studied alloys. The idea is to measure the difference between the means of the batches V1 and V2 in terms of defects and stresses. In statistics, *Cohen's d* is a parameter that quantifies the difference between the means of two populations divided by their standard deviation as a measure to represent the magnitude of mean difference between them. Cohen [47] was the first to introduce this parameter. However, its accuracy relies on two assumptions, the Normality of the distribution and the Homogeneity of variances. In practice, two groups of samples do not necessarily have the same standard deviation. Therefore, to correct the assumption on the Homogeneity of variance, Hedges [48] proposed to use the pooled standard deviation (Eq. 6). Then, the corrected *Cohen's d* is defined as the difference between two means divided by the pooled standard deviation (Eq. 7).

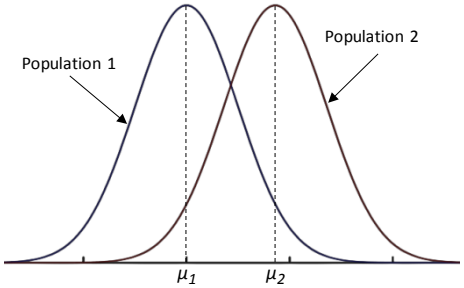

Figure 20: Illustration of two distributions

$$d = \frac{\mu_1 - \mu_2}{s_p} \quad (6)$$

Where, $\boldsymbol{\mu_1}$ and $\boldsymbol{\mu_2}$ are the mean values of the populations.

The pooled standard deviation for the non-equal standard deviation is defined as:

$$S_p = \sqrt{\frac{(n_1 - 1)s_1^2 + (n_2 - 1)s_2^2}{n_1 + n_2 - 2}} \quad (7)$$

Where $\mathbf{n_1}$ and $\mathbf{n_2}$ are the sizes of the populations and $\mathbf{s_1}$ and $\mathbf{s_2}$ are their standard deviations.

In Cohen's terminology, an effect with a small magnitude is an effect that you can see only through a careful study (in terms of number of samples, it takes a relatively large number of samples to reveal it). While, an effect with large magnitude is an effect which is big enough that you may be able to see with the naked eye (otherwise, with a relatively small number of samples you can reveal it). The Table 6 contains descriptors for magnitudes of 'd' from 0.01 to 2.0, as initially suggested by Cohen and expanded by Sawilowsky in 2009 [49].

Table 6: descriptors for magnitudes of d = 0.01 to 2.0, as initially suggested by Cohen and expanded by Sawilowsky

Magnitude of the effect	d	Reference
Very small	0.01	Sawilowsky, 2009
Small	0.20	Cohen, 1988
Medium	0.50	Cohen, 1988
Large	0.80	Cohen, 1988
Very large	1.20	Sawilowsky, 2009
Huge	2.0	Sawilowsky, 2009

Using the experimental data, in the following section we quantify the size effect in terms of defect size and fatigue strength in the studied alloys by calculating the *Cohen's d* of the two populations of the small volume V1 and the standard V2 [Table 7]. We choose those volumes in order to avoid the notch effect.

Table 7 : Summarizes the results in terms of the defect distributions of the standard volumes

	Defect [µm]				Fatigue strength [MPa]			
	A-V1	A-V2	B-V1	B-V2	A-V1	A-V2	B-V1	B-V2
Mean	126	221	352	348	73	65	51	53
Standard Deviation	53	138	100	94	9	8	5	3
Pooled Standard Deviation	101		97		9		4	

From these results in Table 8, the Alloy A present a **large size effect** in terms of defects and fatigue strength. In the other hand, alloy B presents a **very small size effect** in terms of defects and **small size effect** in terms of fatigue strength.

Table 8: Cohen "d" calculation

	Cohen "d"	
	Defect	Fatigue strength
Alloy A	0.93	0.97
Alloy B	0.04	0.45

4. Statistical Analysis of the critical defect and fatigue strength distributions

The aim of this section is to determine which typical statistical distribution (Lognormal, Weibull or Gumbel) is best suited to model the experimental data (i.e. both the fatigue strength distribution and the critical defect size distribution).
Table 9 shows the evaluated probability functions where f is the probability density function (PDF), and F is the cumulative density function (CDF).

In addition, $\phi(x) = \frac{1}{\sqrt{2\pi}}\int_{-\infty}^{x} e^{-\frac{t^2}{2}} dt$ indicates the standard normal cumulative function.

Table 9: evaluated probability functions

Distributions	$\boldsymbol{f(\sigma)}$	$\boldsymbol{F(\sigma)}$
Log-normal	$\frac{1}{\sigma s\sqrt{2\pi}}\exp\left(-\frac{(\ln(\sigma) - \mu)^2}{2\,s^2}\right)$	$\phi\left(\frac{\ln(\sigma) - \mu}{s}\right)$
Weibull	$\frac{\gamma}{\alpha}\left(\frac{\sigma}{\alpha}\right)^{1-\gamma} exp\left[-\left(\frac{\sigma}{\alpha}\right)^{\gamma}\right]$	$1 - exp\left[-\left(\frac{\sigma}{\alpha}\right)^{\gamma}\right]$
Gumbel	$\frac{1}{\beta} exp\left(-\frac{\sigma-\vartheta}{\beta}\right) exp\left[-exp\left(-\frac{\sigma-\vartheta}{\beta}\right)\right]$	$exp\left[-exp\left(-\frac{\sigma-\vartheta}{\beta}\right)\right]$

where μ is the mean and σ is the Standard deviation of logarithmic values for the lognormal distribution. α is the scale parameter and γ is the shape parameter for the Weibull distribution. υ is the location parameter and β is the scale parameter for Gumbel law.

Statistical tests are also used; the Anderson Darling test (AD) combined with its corresponding P-value and the log-likelihood criterion. The reason for choosing the AD test is that in terms of fatigue we are typically interested in the distributions tails, to which the AD test gives greater importance.

To summarize the use of these criteria:

- The best distribution is the one that has the smallest AD value.
- If the corresponding P-value of the AD test is less than α, corresponding to the 5% significance level in this case, then the distribution does not show a good-fit to the data.
- The best distribution is the one that has the highest Log-likelihood value.

Following these criteria, the distributions have been ranked and then the distribution with the best overall rank is chosen. The overall rank is obtained by summation of the individual ranking. The results are presented in table 10.

4.1 Statistics analyses of the defects

Table 10: Summary of the Goodness of Fit (GOF) statistics for different distribution models for the critical defects

Batch	Number of specimens	Tests	Lognormal	Gumbel	Weibull
A-V1	40	P-value	0.58	0.01	0.17
		AD	0.31	1.63	0.54
		Log-likelihood	-222	-232	-224
		Rank	1	3	2
A-V2	37	P-value	0.40	0.01	0.41
		AD	0.38	1.12	0.38
		Log-likelihood	-207	-212	-207
		Rank	1	3	2
A-V3	12	P-value	0.74	0.68	0.90
		AD	0.24	0.28	0.20
		Log-likelihood	-64	-65	-64
		Rank	2	3	1
B-V1	11	P-value	0.78	0.04	0.32
		AD	0.23	0.78	0.43
		Log-likelihood	-59	-62	-61

		Rank	1	3	2
B-V2	11	P-value	0.61	0.38	0.65
		AD	0.28	0.40	0.29
		Log-likelihood	-65	-66	-65
		Rank	1	3	2
Ranking Summary			6	15	9

As shown table 10, the lognormal distribution gives the best approximation for the critical defect size. This conclusion had been made also by YI et al. [50].

Figure 21 shows the experimental data fitted using the lognormal distribution. The parameters of the distribution are obtained using the Maximum Likelihood Estimation method and are summarized in Table 12.

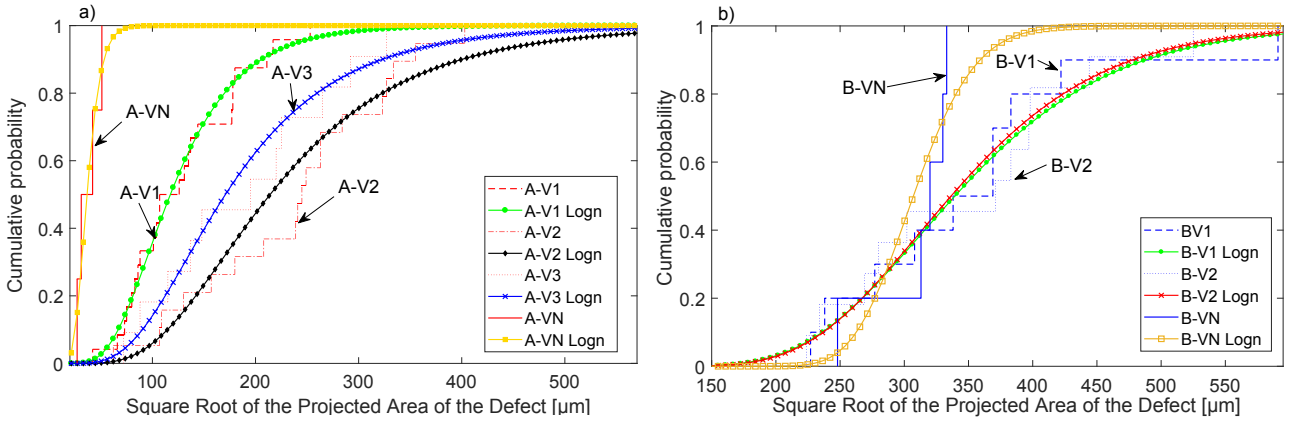

Figure 21: Cumulative probabilities functions of the critical defects for the different tested volumes (a) for alloy A and (b) for alloy B

From Figure 21 (a) it can be seen that (i) for alloy A, the size of critical defects is increased drastically by increasing the size of the FAV. However, for alloy B in Figure 21 (b), the mean values of the distributions for the three different volumes (B-VN, B-V1 and B-V2) are almost the same ($\mu \approx 5.8$ µm) [see Table 12]. These results explain the different sensitivity of alloy A and B fatigue strength to the FAV. In terms of the defect spatial distribution, these results can be explained by the fact that, the largest defects in the alloy A are distributed in a way that when the volume is increased there is a higher probability of finding a large defect. However, for alloy B, the defects are so densely distributed that when increasing the volume of the specimen the probability of finding a large defect does not increase.

4.2 Statistics analyses of the fatigue strength

The same procedure was applied to the data obtained for the fatigue strength. Table 11 summarizes the results of the statistical tests.

Table 11: comparative analyses of the fitting procedure for statistical distribution models of fatigue strength

Batch	Sample size	Creteria	Lognormal	Gumbel	Weibull
A-V1	47	P-value	0.22	0.08	0.20
		AD	0.49	0.66	0.51
		Log-likelihood	-147	-150	-148
		Rank	1	3	2
A-V2	46	P-value	0.01	0.14	0.09
		AD	1.05	0.57	0.65
		Log-likelihood	-125	-124	-124
		Rank	3	1	2
A-V3	11	P-value	0.40	0.01	0.04
		AD	0.36	0.93	0.76
		Log-likelihood	-35	-38	-37

		Rank	1	3	2
B-V1	11	P-value	0.96	0.53	0.72
		AD	0.15	0.33	0.27
		Log-likelihood	-33	-34	-33
		Rank	1	3	2
B-V2	11	P-value	0.38	0.65	0.63
		AD	0.37	0.29	0.30
		Log-likelihood	-27	-26	-26
		Rank	3	1	2
Ranking Summary			9	11	10

From theses analyses, the lognormal distribution was also chosen as the best distribution for the experimental data in terms of fatigue strength distribution for the different batches. The corresponding parameters are summarized in Table 12.

Table 12: summary of the parameters of the identified distributions for 95% confidence level

Batch	Defect						Stress					
	Lognormal		Weibull		Gumbel		Lognormal		Weibull		Gumbel	
A-V1	μ	4.75	α	143	υ	54	μ	4.29	α	77	υ	77
	s	0.43	γ	2.60	β	56.86	s	0.11	γ	9.90	β	7.75
A-V2	μ	5.21	α	230	υ	250	μ	4.16	α	68	υ	68
	s	0.48	γ	2.43	β	93.85	s	0.12	γ	10.13	β	6.48
A-V3	μ	5.14	α	214	υ	230	μ	4.12	α	65	υ	65
	s	0.50	γ	2.58	β	75.75	s	0.10	γ	7.22	β	7.22
B-V1	μ	5.83	α	389	υ	406	μ	3.91	α	52	υ	53
	s	0.28	γ	3.58	β	117.53	s	0.10	γ	11.28	β	4.63
B-V2	μ	5.82	α	382	υ	393	μ	3.93	α	52	υ	52
	s	0.27	γ	4.22	β	90.15	s	0.06	γ	2.08	β	2.08

4.3 Cumulated probability function

In this section, the experimental data are plotted on a lognormal probability scale for the defect size and the fatigue strength distributions :the data should follow a straight line if it conforms to the lognormal distribution [51].

In general, this approach is based on a linearization of the cumulative probability function of the specific distribution. For the lognormal distribution, the cumulative density function can be written as:

$$Y = A + BT \tag{7}$$

Where $Y = \phi^{-1}(F)$ and $T = \ln(\sigma)$ are the variables.

Figure 22 shows lognormal probability paper resulting from this linearized cumulative probability function.

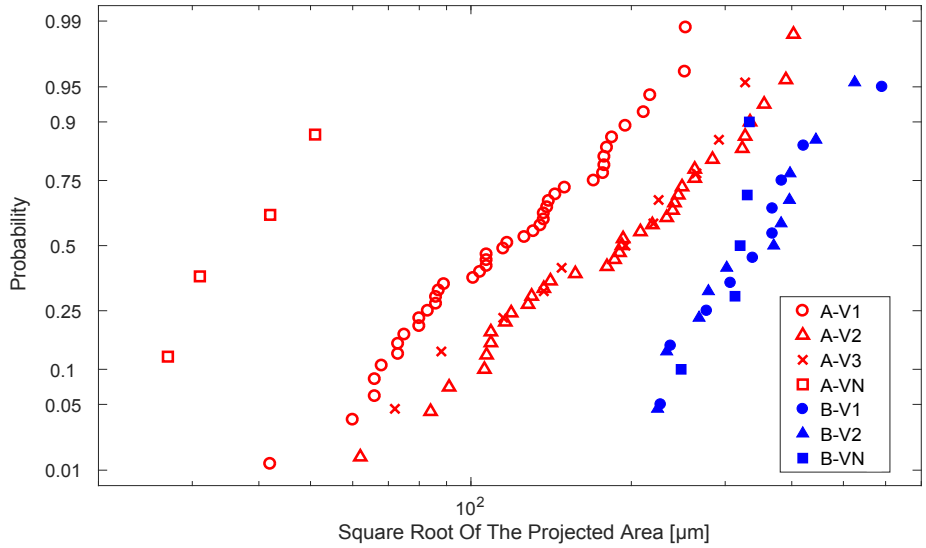

Figure 22: Critical defect sizes in √area plotted on lognormal probability papers

Figure 22 shows the distributions of critical defect sizes in $\sqrt{Area}$ plotted on lognormal probability papers. Firstly, it can be seen that the critical defect sizes show good linearity on the lognormal probability paper. This confirms that the statistical analyses above are correct. Similar results were obtained in [50]. Fig. 19, also shows that, for the three different specimen volumes, the critical defect distribution for alloy B are almost superimposed. This confirms the conclusions from section 3.3. For the case of alloy A, increasing the size of critical volume leads to an increase in the critical defect size, until the A-V2 volume at which the defect size stabilizes.

To sum up, for alloy A, the large defects are rare [see Figure 2]. Therefore, due to the small number of these defects, large defects are unlikely to be found in small specimens (i.e. small critical defects) but are more likely to be found in large specimens. In contrast, alloy B contains a high number of large defects that leads to almost the same probability of finding a large defect in both volumes (B-V1 and B-V2).

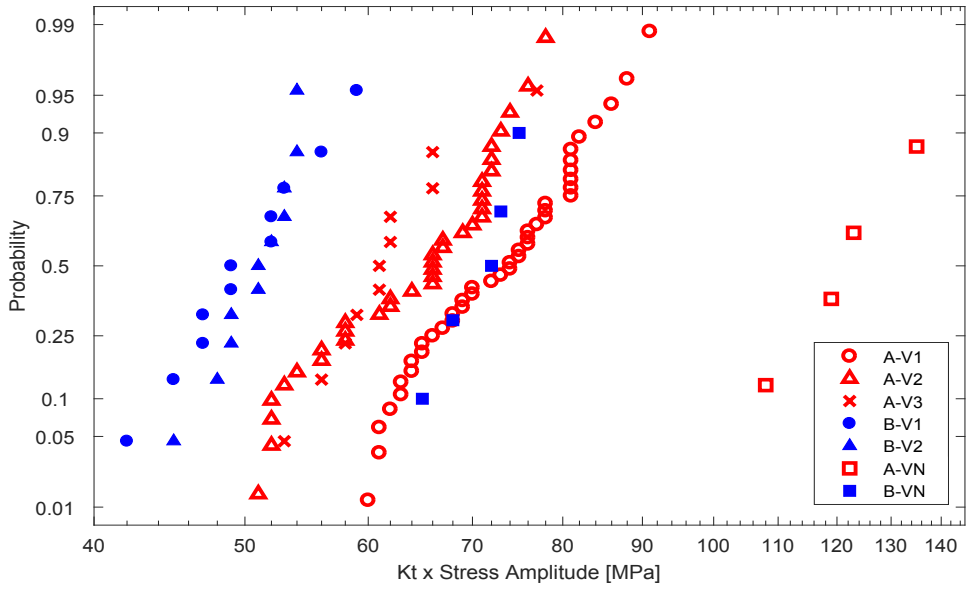

Figure 23: Fatigue strength in MPa plotted on lognormal probability papers

Figure 23 shows that the fatigue strength follows a lognormal distribution. Especially the A-V1 and B-V1 data. This is due to the continuous variation in the section of the V1 specimen shape. In addition to the conclusions drawn in the previous section.

It is very clear thus that the size effect on HCF strength for alloy A is caused by differences in critical defect sizes between different specimens and their spatial distribution. For alloy B, there is an insignificant difference in terms of critical defect sizes between B-V1 and B-V2.

To sum up, the parameters of the distributions of defects in the material (size and spatial distribution) will control the magnitude of the statistical size effect.

- Higher number of large defects and low inter-pores distance leads to non-significant volume effect (case of alloy B): the volume effect is present but has little effect on the observed variables.

- Low number of large defects and relatively large inter-pores distance leads to strong presence of the volume effect which is facilitated by experimental means (case of alloy A).

5. Kitagawa-Takahashi diagram: defect size effect

In order to link the fatigue strength of the different specimens to the critical defect size, Kitagawa-Takahashi diagrams have been established. The estimation of fatigue strength for each specimen was carried out using the local stress. Results are shown in Figure 24.

In this work, the "hot spot" stress at the notch tip is used as a parameter to compare the different configurations. Using classical logic, this implies that Kf is considered equal to Kt, where Kt is the elastic stress concentration factor and Kf is the fatigue notch factor, defined as the ratio of the smooth specimen fatigue strength (reference) to the notched specimen fatigue strength. However, the concept of Kf cannot easily be applied in this work because it has been experimentally shown that the plane specimen fatigue strength is a function of the volume (or the size of the smooth specimen). It is well known that Kf is generally inferior to Kt and that this is often contributed to a "notch effect" which is essentially a combination of the size effect the stress gradient effect and the presence of local plasticity. If the plasticity is considered to be negligible than understanding the notch effect corresponds perfectly to the objectives of this work.
Moreover, given that 1<kf<kt, and Kt=1.78 is not very large, it is expected that the difference between Kt and Kf will not be large.

Figure 24 shows the Kitagawa-Takahashi diagram in terms of local stress amplitude $K_t\sigma_D$ as a function of the square root of the critical defect size. The points on the graph are the critical defects observed on the fatigue failure surfaces of the tested specimens of the two alloys. Note that, for the notched specimens of alloy B (with multi-site initiation), only the largest defect is shown in Figure 24.

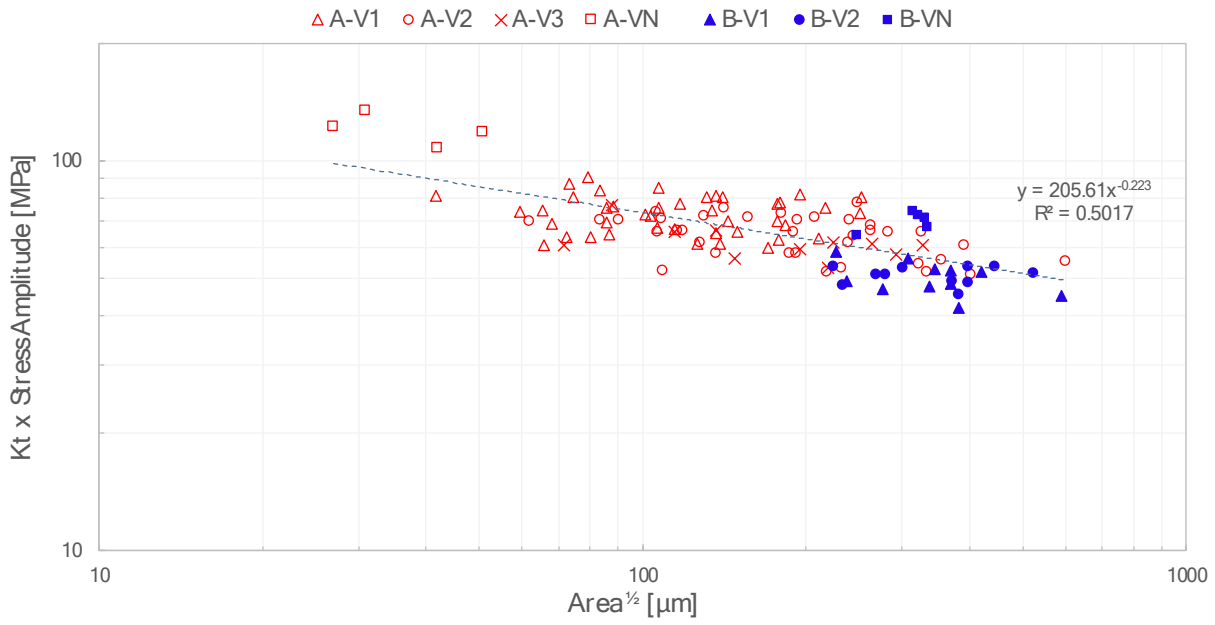

Figure 24: Kitagawa-Takahashi diagram (R=0.1)

From Figure 24, the following conclusions can be made:

i) The fatigue strength of alloy A tends to decrease when the size of the critical defects increases. Same conclusions were made by [11, 12, 18, 35]. Note also that the size of the critical defects increases when the critical volume increases. Indeed, the notched specimens (A-VN) with the lowest critical volume (5 mm^3) have the smallest defect sizes. By changing to a FAV of 110 mm^3 for the A-V1 specimens then to 375 mm^3 for the A-V2 specimens, the size of the critical defects has a tendency to increase and the fatigue strength drops.

ii) Between specimens of size A-V2 and A-V3, there is almost no difference in the average value of the fatigue strength as shown in Figure 12 and Figure 24. It can be concluded that the fatigue strength has stabilised, most probably due to the saturation in the maximum critical defect size.

iii) The size of the critical defects in alloy B is relatively large for all types of tested specimens. Their $\sqrt{Area}$ are greater than 220 µm. For this range of defect size, the fatigue strength of the specimens does not change significantly compared to the variation in alloy A.

Using the Kitagawa-Takahashi diagram represented with linear axes Figure 25 gives a better understanding of the small size effect in alloy B. The critical defects are generally at the level where the fatigue strength begins to stabilize. Therefore, and since the size of the critical defects remain relatively large ($\sqrt{Area}$ greater than 220 µm), the difference in the fatigue strength and the scatter remain low. Indeed, when the size goes from 220 µm to 620 µm the local stress amplitude goes from approximately 67 MPa to 60 MPa [see Figure 25]. So, even for the different specimen sizes, the fatigue strength does not significantly change leading to a slight size effect and a low scatter.

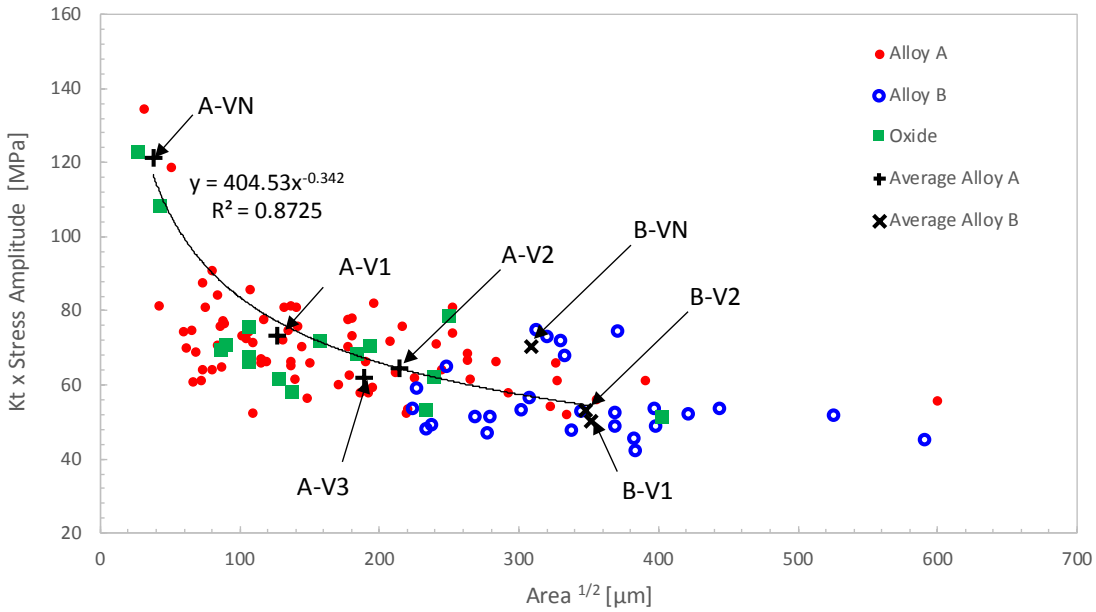

Figure 25: Local fatigue resistance as a function of critical defect size (R=0.1)

Figure 26 is a schematic representation of the fatigue strength amplitude as a function of the average critical defect size for volumes A-V1, A-V2, B-V1 and B-V2. It shows that due to the large average critical defect size of the alloy B, The size effect and the scatter are low. In contrast, the average critical defect size of the A-V1 and A-V2 specimens are in the interval in which the curve has a strong slope. A large difference between the fatigue strength of these two volumes and high scatter can hence be expected.

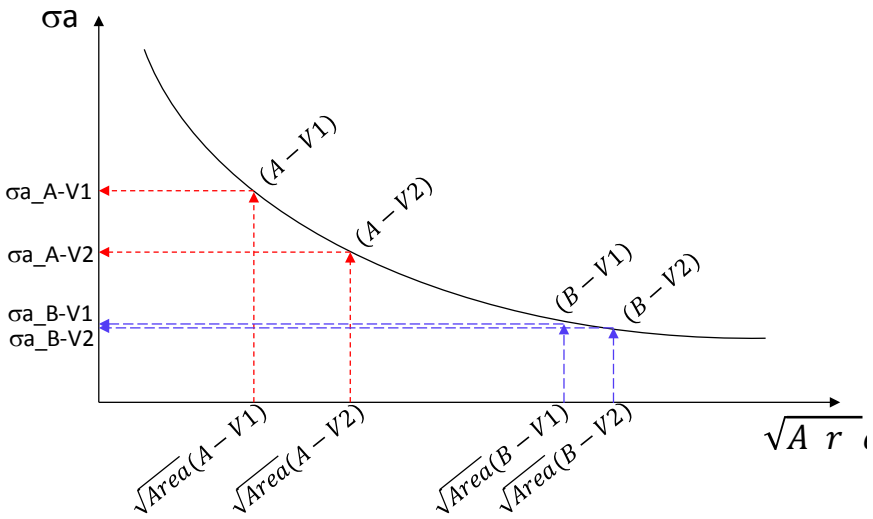

Figure 26: Schematic representation of fatigue resistance as a function of the means of critical defect size for each batch

A large size effect in terms of fatigue strength is a result of large size effect in the corresponding distributions of critical defect size (which is the case for alloy A). However, a large size effect if terms of critical defects does not lead systematically to a large size effect in terms of fatigue strength, depending on the range of the critical defect size.

6. Study of the notch effect

As previously discussed, four of the five specimens tested from batch B-VN, have two crack initiation sites (see Figure 15 and Table 4). In this section, the notch effect is investigated for both alloys. Computer Tomography analyses are used to gain insight into the problem.

6.1 Post-mortem analyses

As shown in Figure 27, the defect density and the size of the defects in the notched section of the specimen taken from alloy B are much higher in comparison with alloy A.

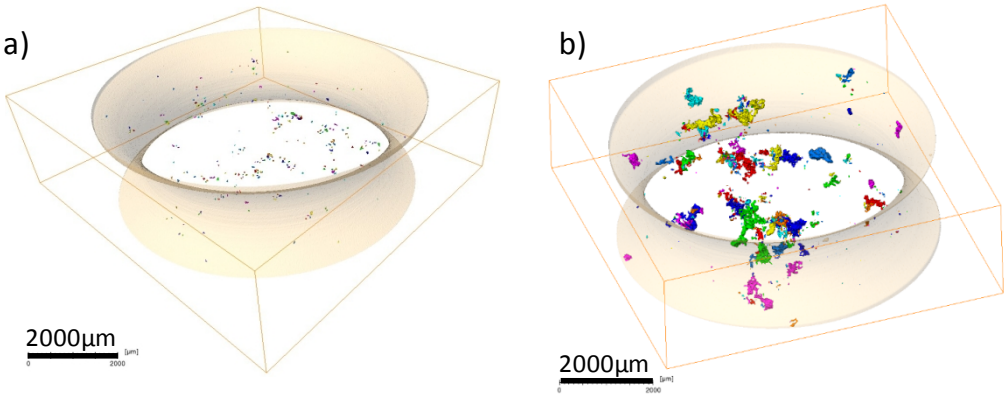

Figure 27: CT scans of the notched section of (a) specimen A-VN-05, and (b) specimen B-VN-05

Figure 28 shows the location of the defects in the notched specimens A-VN-05 and B-VN-05 as a function of their sizes in terms of $\sqrt{Area}_{eq}$.

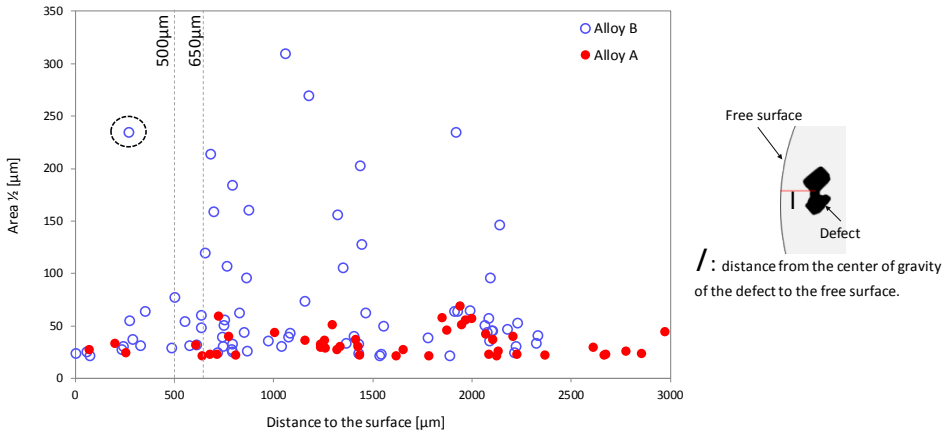

Figure 28: The size of defects contained in the notched section and their location to the surface

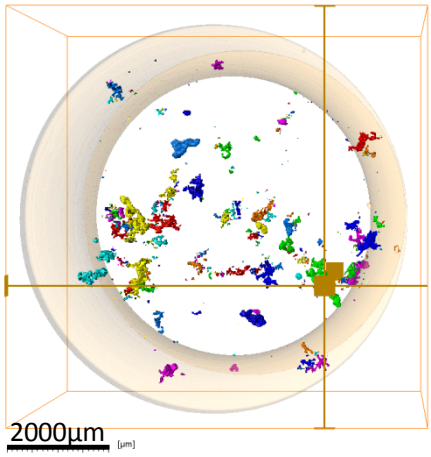

Figure 29: The location of the encircled defect in Figure 28

From Figure 28 and Figure 29, two important conclusions can be made; (i) firstly there is a higher number of defects in the subsurface of the B-VN-05 specimen (10 defects) when compared to the A-VN-05 specimen (3 defects). (ii) Secondly, the largest defect in the FAV for alloy B is almost 7 times larger than the largest defect in alloy A in terms of $\sqrt{Area}_{eq}$. The largest defect size in the alloy B notched specimen is about $\sqrt{Area}_{eq} \approx 200\ \mu m$ and for the alloy A is about $\sqrt{Area}_{eq} \approx 35\ \mu m$.

The high defect density in alloy B means that even by decreasing the FAV, there is still a high probability of finding large defects near to the surface of the notch. This explains why the averages of the distributions for alloy B in Figure 21 are close to each other for different FAVs. The opposite is observed for alloy A. By decreasing the FAV, the average size of the critical defect drops (see Figure 19). This leads to the activation of other failure mechanisms such as oxide, inclusion or PSB.

Furthermore, the higher probability of finding many large defects near to the surface of the notch in alloy B can lead to the multiple crack initiation sites. Two crack initiation sites were observed in four out of five notched specimens for batch B-VN. This phenomenon is also linked to the gradient stress effect introduced by the notch.

6.2 Crack initiation at the notch

In the following, the fractographic analyses have been matched to the tomographic analyses, the results are shown in Figure 30 and Figure 31.

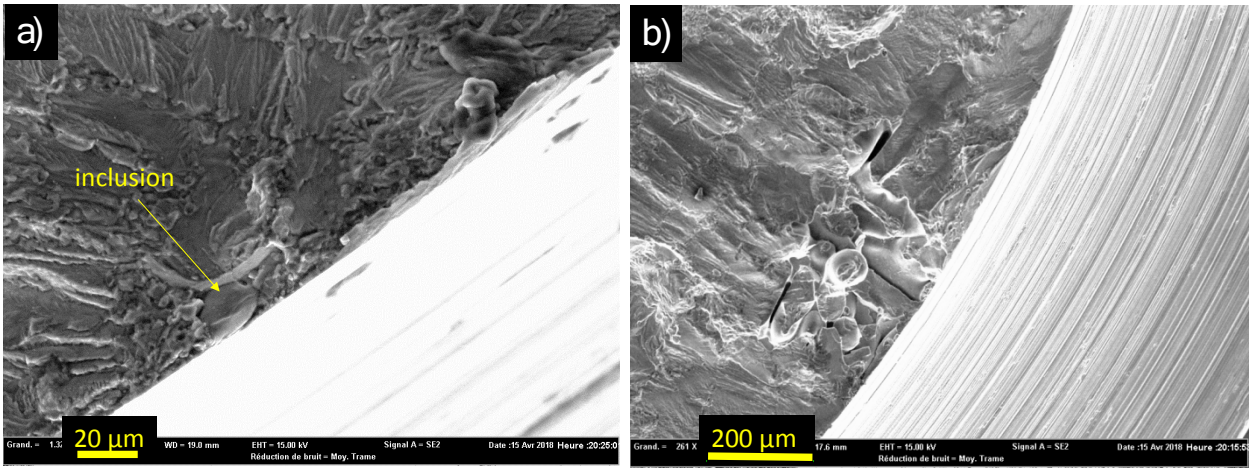

Figure 30: Fatigue failure, (a) specimen A-VN-05, Sa=70 MPa, Nf=1584002 cycles, crack initiation from an inclusion with $\sqrt{\boldsymbol{Area}}$ of 27 µm (b) specimen B-VN-05, Sa=45 MPa, Nf=777402 cycles and crack initiation from a pore at the surface with $\sqrt{\boldsymbol{Area}}$ of 313 µm

For alloy A, the results show that due to the lack of large defects near the surface, the specimen has failed from an inclusion located at the surface. For alloy B, due to the high density of large pores in this material, the specimen has failed from a pore at the surface. It can be seen that the critical pore is not the largest one contained in the fatigue active volume, as indicated in Figure 29. It is a different pore at the surface of the notch (see Figure 30 (b) and Figure 31).

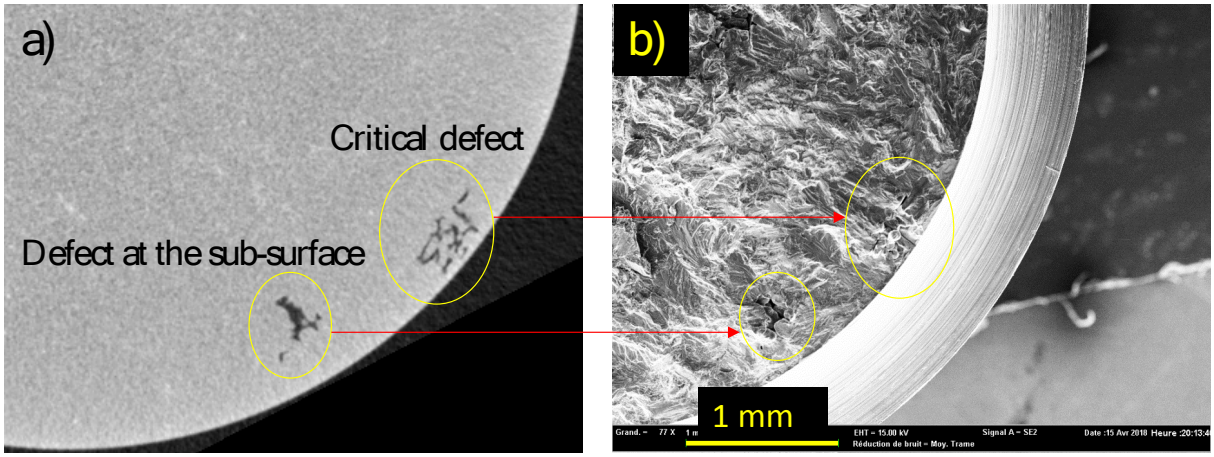

Figure 31: specimen B-VN-05 (a) tomographic image and (b) its corresponding fractographic image

7. Conclusions

In this study, an experimental investigation has been conducted to evaluate the statistical size effect (or volume eff ect) on the fatigue strength of cast Al-Si alloys. Statistical analyses of fatigue data were carried out by means of statistical tests (Log-likelihood, AD test and its corresponding P-value). The main results can be summarized as follows:

- The fatigue strength is strongly dependent on microstructure defects in cast aluminium alloys. The most harmful defects are the pores located on specimen surface or subsurface. The pore size is the key factor controlling fatigue strength, and the random distribution of pores can cause great scatter in fatigue strength.
- A variation in the highly stressed volume is accompanied by a change in the fatigue strength of the material. This result confirms the existence of a size effect in cast Al-Si alloys. Furthermore, alloy A has a more

pronounced volume effect than alloy B. This is due to the characteristics of the defect population of each alloy (pore size and distance between large pores).
- Good correlation between the local fatigue strength amplitude $K_t\sigma_D$ and the critical volume was found. Hence, it can be concluded that the highly stressed volume approach is an effective way to describe the statistical size effect in cast Al-Si alloys.
- Both critical defects size and the fatigue strength follow a lognormal distribution. For the fatigue strength, this has consequences for fatigue design. Some works are based on the idea that the fatigue resistance follows a normal distribution [53]. Which is not the case for Al-Si cast alloys.
- The fatigue strength for alloy A stabilizes from a critical volume of 375 mm^3, which can be considered as the Fatigue Representative Elementary Volume.
- The fatigue strength of alloy B stabilizes at a smaller critical volume of 110 mm^3 which can be considered as the fatigue REV of this alloy.
- The alloys do not show the same fatigue damage mechanisms. For the alloy B, all the specimens have shown fracture initiated from a pore. However, the alloy A shows several mechanisms of crack initiation (pores, oxide, PSB). Nevertheless, the initiation from the pore is the predominant mechanisms and the percentage of the other mechanisms increases by decreasing the FAV size.
- Size effect and scatter of fatigue are strongly linked to the average size of the critical defects. If the average size of the critical defect is lower than 220 µm, the alloy will show high size effect and high scatter, which is the case of alloy A. If it is higher than 220 µm the alloy will show low size effect and low scatter, that is the case of alloy B.
- Density of pores plays a role also in the fatigue size effect and scatter; more presence of large defects and low inter-pores distance (high-density) leads to non-significant volume effect (case of alloy B). On the other hand, less presence of large defects and relatively large inter-pores distance (low-density) leads to strong presence of the volume effect (case of alloy A).

A modelling work coupling the defect size and position distributions and the loaded volume is in progress and will be presented in a next paper.

Groupe PSA and the French National Agency for Research and Technology (ANRT) financially supported this work.

References

[1] D. A. Kelly et J. L. M. Morrison, « Effect of Specimen Size and Preparation on the Fatigue Strength of a Plain Carbon Steel Tested in Rotating Bending and in Torsion », *Proc. Inst. Mech. Eng.*, vol. 185, nº 1, p. 655‑664, juin 1970.
[2] A. Carpinteri, Spagnoli, Andrea, et Vantadori, Sabrina, « Size effect in S–N curves: A fractal approach to finite-life fatigue strength ».
[3] K. H. Kloos, A. Buch, et D. Zankov, « Pure Geometrical Size Effect in fatigue tests with constant stress amplitude and in programme tests », *Mater. Werkst.*, vol. 12, nº 2, p. 40‑50, févr. 1981.
[4] M. Makkonen, « Size Effect and Notch Size Effect in Metal Fatigue », août 1999.
[5] W. Weibull, *The phenomenon of rupture in solids,*. Stockholm: Generalstabens litografiska anstalts förlag, 1939.
[6] I. V. Papadopoulos et V. P. Panoskaltsis, « Invariant formulation of a gradient dependent multiaxial high-cycle fatigue criterion », *Eng. Fract. Mech.*, vol. 55, nº 4, p. 513‑528, nov. 1996.
[7] L. Flaceliere et F. Morel, « Probabilistic approach in high-cycle multiaxial fatigue: volume and surface effects », *Fatigue Fract. Eng. Mater. Struct.*, vol. 27, nº 12, p. 1123‑1135, 2004.
[8] F. Abroug, E. Pessard, G. Germain, et F. Morel, « A probabilistic approach to study the effect of machined surface states on HCF behavior of a AA7050 alloy », *Int. J. Fatigue*, vol. 116, p. 473‑489, nov. 2018.
[9] N. Saintier, T. Palin-luc, J. Bénabes, et F. Cocheteux, « Non-local energy based fatigue life calculation method under multiaxial variable amplitude loadings », *Int. J. Fatigue*, vol. 54, p. 68‑83, sept. 2013.

[10] A. Banvillet, T. Palin-Luc, et S. Lasserre, « A volumetric energy based high cycle multiaxial fatigue citerion », *Int. J. Fatigue*, vol. 25, nº 8, p. 755‑769, août 2003.
[11] R. Hidalgo, J. A. Esnaola, I. Llavori, M. Larrañaga, I. Hurtado, et N. Herrero-Dorca, « Fatigue life estimation of cast aluminium alloys considering the effect of porosity on initiation and propagation phases », *Int. J. Fatigue*, vol. 125, p. 468‑478, août 2019.
[12] J. Tenkamp, A. Koch, S. Knorre, U. Krupp, W. Michels, et F. Walther, « Defect-correlated fatigue assessment of A356-T6 aluminum cast alloy using computed tomography based Kitagawa-Takahashi diagrams », *Int. J. Fatigue*, vol. 108, p. 25‑34, mars 2018.
[13] H. R. Ammar, A. M. Samuel, et F. H. Samuel, « Effect of casting imperfections on the fatigue life of 319-F and A356-T6 Al–Si casting alloys », *Mater. Sci. Eng. A*, vol. 473, nº 1, p. 65‑75, janv. 2008.
[14] F. Menan, P.-A. Adragna, et M. François, « The Stress-Strength Interference Method Applied to Fatigue Design: The Independence of the Random Variables », *Procedia Eng.*, vol. 133, p. 746‑757, janv. 2015.
[15] F. Abroug, E. Pessard, G. Germain, et F. Morel, « HCF of AA7050 alloy containing surface defects: Study of the statistical size effect », *Int. J. Fatigue*, vol. 110, p. 81‑94, mai 2018.
[16] Chantier, Bobet, Billardon, et Hild, « A probabilistic approach to predict the very high-cycle fatigue behaviour of spheroidal graphite cast iron structures », *Fatigue Fract. Eng. Mater. Struct.*, vol. 23, nº 2, p. 173‑180, 2000.
[17] V.-D. Le, F. Morel, D. Bellett, N. Saintier, et P. Osmond, « Multiaxial high cycle fatigue damage mechanisms associated with the different microstructural heterogeneities of cast aluminium alloys », *Mater. Sci. Eng. A*, vol. 649, p. 426‑440, janv. 2016.
[18] E. Pessard, F. Morel, C. Verdu, L. Flacelière, et G. Baudry, « Microstructural heterogeneities and fatigue anisotropy of forged steels », *Mater. Sci. Eng. A*, vol. 529, p. 289‑299, nov. 2011.
[19] E. Pessard, F. Morel, A. Morel, et D. Bellett, « Modelling the role of non-metallic inclusions on the anisotropic fatigue behaviour of forged steel », *Int. J. Fatigue*, vol. 33, nº 4, p. 568‑577, avr. 2011.
[20] I. Koutiri, D. Bellett, F. Morel, L. Augustins, et J. Adrien, « High cycle fatigue damage mechanisms in cast aluminium subject to complex loads », *Int. J. Fatigue*, vol. 47, p. 44‑57, févr. 2013.
[21] V. D. Le, « Etude de l'influence des hétérogénéités microstructurales sur la tenue en fatigue à grand nombre de cycles des alliages d'aluminium de fonderie », Thèse de doctorat, Arts et Métiers ParisTech, France, 2016.
[22] I. Koutiri, « Effet des fortes contraintes hydrostatiques sur la tenue en fatigue des matériaux métalliques », Thèse de doctorat, Arts et Métiers ParisTech, France, 2011.
[23] P. Osmond, V.-D. Le, F. Morel, D. Bellett, et N. Saintier, « Effect of porosity on the fatigue strength of cast aluminium alloys: from the specimen to the structure », *Procedia Eng.*, vol. 213, p. 630‑643, janv. 2018.
[24] M. M. Jan, H.-P. Gaenser, et W. Eichlseder, « Prediction of the low cycle fatigue regime of the S–N curve with application to an aluminium alloy », *Proc. Inst. Mech. Eng. Part C J. Mech. Eng. Sci.*, vol. 226, nº 5, p. 1198‑1209, mai 2012.
[25] R. Kuguel, « A relation between theoretical stress concentration factor and fatigue notch factor deduced from the concept of highly stressed volume », *ASTM Proc*, vol. 61, p. 732‑748, 1961.
[26] C. M. Sonsino et G. Fischer, « Local Assessment Concepts for the Structural Durability of Complex Loaded Components », *Mater. Werkst.*, vol. 36, nº 11, p. 632‑641, 2005.
[27] C.-K. Lin et W.-J. Lee, « Effects of highly stressed volume on fatigue strength of austempered ductile irons », *Int. J. Fatigue*, vol. 20, nº 4, p. 301‑307, avr. 1998.
[28] C. M. Sonsino et E. Moosbrugger, « Fatigue design of highly loaded short-glass-fibre reinforced polyamide parts in engine compartments - », juill-2008. .
[29] Y. Ai *et al.*, « Probabilistic modeling of fatigue life distribution and size effect of components with random defects », *Int. J. Fatigue*, vol. 126, p. 165‑173, sept. 2019.
[30] Y. Ai, S.-P. Zhu, D. Liao, J. A. F. O. Correia, A. M. P. De Jesus, et B. Keshtegar, « Probabilistic modelling of notch fatigue and size effect of components using highly stressed volume approach », *Int. J. Fatigue*, vol. 127, p. 110‑119, oct. 2019.
[31] S.-P. Zhu, S. Foletti, et S. Beretta, « Evaluation of size effect on strain-controlled fatigue behavior of a quench and tempered rotor steel: Experimental and numerical study », *Mater. Sci. Eng. A*, vol. 735, p. 423‑435, sept. 2018.
[32] G. Antaki et R. Gilada, « Chapter 1 - Regulations, Codes, and Standards », in *Nuclear Power Plant Safety and Mechanical Integrity*, G. Antaki et R. Gilada, Éd. Boston: Butterworth-Heinemann, 2015, p. 1‑26.

[33] G. Antaki et R. Gilada, « Chapter 2 - Design Basis Loads and Qualification », in *Nuclear Power Plant Safety and Mechanical Integrity*, G. Antaki et R. Gilada, Éd. Boston: Butterworth-Heinemann, 2015, p. 27‑102.
[34] A. Hirano, M. Nakane, S. Asada, et T. Sera, « Study on Consideration of Size Effects on Design Fatigue Curve », p. V001T01A029, juill. 2014.
[35] M. Iben Houria, Y. Nadot, R. Fathallah, M. Roy, et D. M. Maijer, « Influence of casting defect and SDAS on the multiaxial fatigue behaviour of A356-T6 alloy including mean stress effect », *Int. J. Fatigue*, vol. 80, p. 90‑102, nov. 2015.
[36] A. Ben Ahmed, A. Nasr, A. Bahloul, et R. Fathallah, « The impact of defect morphology, defect size, and SDAS on the HCF response of A356-T6 alloy », *Int. J. Adv. Manuf. Technol.*, vol. 92, nº 1, p. 1113‑1125, sept. 2017.
[37] I. Serrano-Munoz, J.-Y. Buffiere, R. Mokso, C. Verdu, et Y. Nadot, « Location, location & size: defects close to surfaces dominate fatigue crack initiation », *Sci. Rep.*, vol. 7, p. 45239, mars 2017.
[38] J.-Y. Buffière, S. Savelli, P. H. Jouneau, E. Maire, et R. Fougères, « Experimental study of porosity and its relation to fatigue mechanisms of model Al–Si7–Mg0.3 cast Al alloys », *Mater. Sci. Eng. A*, vol. 316, nº 1, p. 115‑126, nov. 2001.
[39] T. Schlömer, D. Heck, et O. Deussen, « Farthest-point optimized point sets with maximized minimum distance », in *Proceedings of the ACM SIGGRAPH Symposium on High Performance Graphics - HPG '11*, Vancouver, British Columbia, Canada, 2011, p. 135.
[40] C. Garb, M. Leitner, M. Tauscher, M. Weidt, et R. Brunner, « Statistical analysis of micropore size distributions in Al–Si castings evaluated by X-ray computed tomography », *Int J Mater Res*, p. 11, 2018.
[41] I. Boromei, L. Ceschini, A. Morri, A. Morri, G. Nicoletto, et E. Riva, « Influence of the solidification microstructure and porosity on the fatigue strength of Al-Si-Mg casting alloys », vol. 28, p. 7, 2010.
[42] P. Mu, Y. Nadot, C. Nadot-Martin, A. Chabod, I. Serrano-Munoz, et C. Verdu, « Influence of casting defects on the fatigue behavior of cast aluminum AS7G06-T6 », *Int. J. Fatigue*, vol. 63, p. 97‑109, juin 2014.
[43] A. Rotella, Y. Nadot, M. Piellard, et R. Augustin, « Influence of natural defects on the fatigue limit of a cast Al-Si alloy », *Procedia Struct. Integr.*, vol. 7, p. 513‑520, janv. 2017.
[44] T. Engelke et A. Esderts, « Analytical strength assessments of austempered ductile iron components », p. 5, 2018.
[45] K. Lipp, J. Baumgartner, et P. Beiss, « Fatigue design of sintered steel components: effect of stress concentrations and mean stresses on local strength using highest stressed volume approach », *Powder Metall.*, vol. 56, nº 5, p. 337‑341, déc. 2013.
[46] D. B. Lanning, T. Nicholas, et G. K. Haritos, « On the use of critical distance theories for the prediction of the high cycle fatigue limit stress in notched Ti–6Al–4V », *Int. J. Fatigue*, vol. 27, nº 1, p. 45‑57, janv. 2005.
[47] J. Cohen, *Statistical power analysis for the behavioral sciences*. Hillsdale, N.J.: L. Erlbaum Associates, 1988.
[48] L. V. Hedges, « Estimation of effect size from a series of independent experiments », *Psychol. Bull.*, vol. 92, nº 2, p. 490‑499, 1982.
[49] S. Sawilowsky, « New Effect Size Rules of Thumb », *J. Mod. Appl. Stat. Methods*, vol. 8, nº 2, nov. 2009.
[50] J. Z. Yi, Y. X. Gao, P. D. Lee, H. M. Flower, et T. C. Lindley, « Scatter in fatigue life due to effects of porosity in cast A356-T6 aluminum-silicon alloys », *Metall. Mater. Trans. A*, vol. 34, nº 9, p. 1879, sept. 2003.
[51] K. J. Koehler, « Goodness-of-Fit Tests Based on P-P Probability Plots AU - Gan, F. F. », *Technometrics*, vol. 32, nº 3, p. 289‑303, août 1990.
[52] Y. Murakami, *Metal Fatigue: Effects of Small Defects and Nonmetallic Inclusions*. Elsevier, 2002.
[53] J. J. Thomas, G. Perroud, A. Bignonnet, et D. Monnet, « Fatigue design and reliability in the automotive industry », in *European Structural Integrity Society*, vol. 23, G. Marquis et J. Solin, Éd. Elsevier, 1999, p. 1‑11.

Appendix: Staircase tables

N°	R	0.1	0.1	0.1	0.1	0.1	0.1	0.1	0.1	0.1	0.1	0.1	
	σ_{MPa}	95	90	85	80	75	70	65	60	55			Nf
A-V1-01								X	O	O			1048913
A-V1-02						X	O	O	O				99555
A-V1-03						X	O	O					1873042
A-V1-04					X	O	O						1228247
A-V1-05			X	O	O	O							1264571
A-V1-06	X	O	O	O									350867
A-V1-07				X									295150
A-V1-08				X	O								529235
A-V1-09				X									503900
A-V1-10					X								659570
A-V1-11			X	O	O	O							1031132
A-V1-12					X								314844
A-V1-13	X	O	O	O	O	O							344861
A-V1-14		X	O	O	O								207326
A-V1-15				X									330879
A-V1-16				X	X	O							1615089
A-V1-17				X	X	O							388060
A-V1-18					X								1066691
A-V1-19						X							1256599
A-V1-20						X	O						922224
A-V1-21					X	O	O						411741
A-V1-22					X	O							830867
A-V1-31				X									305048
A-V1-23					X								271095
A-V1-24			X	O	O	O							297233
A-V1-25					X								379160
A-V1-26						X							1834795
A-V1-27						X	O						84737
A-V1-32						X							1504674
A-V1-28							X						325756
A-V1-29								X					1255402
A-V1-30								X	O				483099
A-V1-33								X					624228
A-V1-34						X	O	O	O				1658253
A-V1-35					X	O	O	O					1099695
A-V1-36							X						1028621
A-V1-37								X					1945197
A-V1-38							X	O	O				1567963
A-V1-39								X					361970
A-V1-40									X				1995662
A-V1-41							X	O	O	O			1743252
A-V1-42							X	O	O				1292279
A-V1-43								X					1581225
A-V1-44					X	O	O	O	O				545162
A-V1-45							X	O					89110
A-V1-46							X						854130
A-V1-47								X					1567256

N°	R	0.1	0.1	0.1	0.1	0.1	0.1	0.1	
	σ_a (MPa)	80	75	70	65	60	55	50	Nf
A-V2-01							X		520971
A-V2-02							X	O	1724321
A-V2-03						X	O		392140
A-V2-04						X			231463
A-V2-05							X		733008
A-V2-06					X	O	O	O	1663959
A-V2-07	Failed at the head						O		
A-V2-08				X	O	O			1999900
A-V2-09			X	O	O				872751
A-V2-10	X	O	O	O					2014781
A-V2-11			X						358960
A-V2-12				X					297730
A-V2-13					X				764058
A-V2-14	X	O	O	O	O	O			2000002
A-V2-15				X	O				569436
A-V2-16				X					648430
A-V2-17				X	O				441454
A-V2-18			X	O					482700
A-V2-19			X						817570
A-V2-20				X					1432995
A-V2-21					X				1497443
A-V2-22	X	O	O	O	O	O			428882
A-V2-23			X	O	O				1351305
A-V2-24			X	O					123718
A-V2-25			X						639271
A-V2-26			X	O					1179764
A-V2-27	X	O							1350016
A-V2-28	X								291023
A-V2-29		X							328135
A-V2-30			X						435331
A-V2-31				X					1081376
A-V2-32					X				1147932
A-V2-33					X	O			1196663
A-V2-34					X				1160947
A-V2-35						X			900176
A-V2-36					X	O	O		1391975
A-V2-37						X			867672
A-V2-38						X	O		1320201
A-V2-39				X	O	O	O		34182
A-V2-40					X	O			693812
A-V2-41					X				380204
A-V2-42				X	O	O			221300
A-V2-43				X	O				602003
A-V2-44			X	O					1656020
A-V2-45			X						207862
A-V2-46				X					424055

N°		B-V2-11	B-V2-10	B-V2-9	B-V2-8	B-V2-7	B-V2-6	B-V2-5	B-V2-4	B-V2-3	B-V2-2	B-V2-1
σ_a MPa	R											
55	0.1	x	x		x	x	x	x	x			
50	0.1	o	o	x		o		o	o	x	x	x
45	0.1		o						o	o	o	o
40	0.1									o	o	o
35	0.1										o	o
30	0.1											o
Nf		471485	1418384	1205756	1729483	1214144	422845	603598	1386581	180706	1522169	1715287

N°		B-VN-05	B-VN-04	B-VN-03	B-VN-02	B-VN-01
σa MPa	R					
45	0.1	X	X	X		
40	0.1	O	O	O	X	X
35	0.1		O	O	O	O
30	0.1				O	O
Nf		777402	129663	390896	1249259	590639

N°		A-VN-05	A-VN-04	A-VN-03	A-VN-02	A-VN-01
σa MPa	R					
80				X		
75	0.1			O		
70	0.1	X		O	X	X
65	0.1	O	X	O	O	O
60	0.1	O			O	O
55	0.1					O
50	0.1					O
Nf		1584002	287762	239540	356006	690648

N°		B-V1-11	B-V1-10	B-V1-9	B-V1-8	B-V1-7	B-V1-6	B-V1-5	B-V1-4	B-V1-3	B-V1-2	B-V1-1
σ_a MPa	R											
60	0.1						x					x
55	0.1					x	o	x	x			o
50	0.1		x	x	x		o		o	x	x	o
45	0.1	x		o						o	o	o
40	0.1										o	o
35	0.1											o
Nf		860126	1609297	697638	993818	781765	503757	919402	1067352	1368021	1433516	1494524

N°		A-V3-12	A-V3-11	A-V3-10	A-V3-09	A-V3-08	A-V3-07	A-V3-06	A-V3-05	A-V3-04	A-V3-03	A-V3-02	A-V3-01
σ_a MPa	R												
80	0.1									x			Failed at the head
75	0.1									o			
70	0.1						x			o	x		
65	0.1	x	x			x	o	x		o	o		
60	0.1		o	x	x		o	o	x	o	o		x
55	0.1			o				o		o	o	x	o
50	0.1										o		o
Nf		437907	684272	1718933	476402	632926	458688	425443	1080523	827135	316000	1333158	926468

Highlights

- Effects of porosity on size effect and scatter of fatigue strength are investigated.
- Two alloys with different degrees of porosity are used.
- Magnitude of size effect and scatter are linked to the population defects.
- High density and large size defects lead to minor size effect and less scatter.
- Low density and small size defects induce large size effect and high scatter.